

Geodetic VLBI Observations of EGRET Blazars

B. Glenn Piner^{1,2}

NASA/Goddard Space Flight Center, Code 661, Greenbelt, MD 20771

Kerry A. Kingham

U.S. Naval Observatory, Earth Orientation Dept., 3450 Massachusetts Ave, Washington
D.C. 20392

ABSTRACT

We present VLBI observations of the EGRET quasars 0202+149, CTA 26, and 1606+106, as well as additional analysis of VLBI observations of 1156+295 presented in Piner & Kingham (1997b). We have produced 8 and 2 GHz VLBI images at 11 epochs, 8 epochs, and 12 epochs, spanning the years 1989 to 1996, of 0202+149, CTA 26, and 1606+106 respectively. The VLBI data have been taken from the Washington VLBI correlator's geodetic database. We have measured the apparent velocities of the jet components and find that CTA 26 and 1606+106 are superluminal sources, with average apparent speeds of 8.9 and 2.9 $h^{-1}c$ respectively ($H_0 = 100h$ km s⁻¹ Mpc⁻¹, $q_0=0.5$). The components in 0202+149 are stationary, and we identify this source as a compact F double. These sources all have apparently bent jets, and we detected non-radial motion of components in CTA 26 and 1156+295. We have not yet detected any components emerging subsequent to the γ -ray flares in CTA 26, 1156+295, and 1606+106, and we derive lower limits on the ejection times of any such components. The misalignment angle distribution of the EGRET sources is compared to the distribution for blazars as a whole, and we find that EGRET sources belong preferentially to neither the aligned nor the misaligned population. We also compare the average values for the apparent velocities and Doppler beaming factors for the EGRET and non-EGRET blazars, and find no significant differences. We thus find no indication, within the measurement errors, that EGRET blazars are any more strongly beamed than their counterparts which have not been detected in γ -rays.

¹Department of Astronomy, University of Maryland, College Park MD 20742

²currently at: California Institute of Technology, Jet Propulsion Laboratory, 4800 Oak Grove Dr., M-S: 238-332, Pasadena, CA 91109

Subject headings: Galaxies: Jets - Quasars: Individual (0202+149, CTA 26, 1156+295, & 1606+106) - Radio Continuum: Galaxies

1. Introduction

Since its launch in 1991, the EGRET instrument on the *Compton Gamma Ray Observatory* (CGRO) has detected with high significance 51 AGNs as emitters of high energy γ -rays (Mukherjee et al. 1997). These sources all appear to be members of the blazar class of AGNs (von Montigny et al. 1995a), containing BL Lac objects, highly polarized quasars (HPQ), and optically violent variable (OVV) quasars. In the radio these AGNs are radio-loud and flat-spectrum (radio spectral index $\alpha \geq -0.5$). The γ -ray emission from these sources has notable properties, including high γ -ray flux that in many of the sources dominates the flux at lower energies, and rapid variability on timescales of a few days or less (e.g. von Montigny et al. 1995a). The high γ -ray flux and rapid time variability have been used to argue that the γ -ray emission must be relativistically beamed; if not, the γ -ray emission would be attenuated by pair-production optical depth. Significant Doppler beaming factors for EGRET sources have been derived by this method by e.g. Mattox et al. (1993) and Doni & Ghisellini (1995).

In the relativistic beaming model, the γ -ray sources are strongly beamed and should display certain distinct properties when imaged with VLBI, including apparent superluminal motion of jet components, a high degree of core dominance, and jets which are strongly bent by projection effects. Some of the EGRET sources had been well monitored with VLBI before their detection by EGRET, and they did indeed display these properties. Proper motion measurements for 13 EGRET sources are listed by Vermeulen & Cohen (1994), hereafter VC94. The measured apparent velocities of these sources are all superluminal (provided the redshift of 0716+714 is above 0.28), with the exceptions of 0458-020, 1127-145, and CTA 102. VLBI observations of other sources have been spurred by their EGRET detections, and superluminal motion has recently been reported in 0420-014 (Wagner et al. 1995), 0528+134 (Krichbaum et al. 1995; Pohl et al. 1995), 0954+658 and 1219+285 (Gabuzda et al. 1994), 1633+382 (Barthel et al. 1995), and 1730-130 (Bower et al. 1997). A campaign to monitor the southern EGRET sources with VLBI is underway, with first results reported by Tingay et al. (1996).

The fact that many of the EGRET sources were relatively obscure until their detection by EGRET indicates that, despite the recent concentration on VLBI observations of EGRET sources, there remain many γ -ray sources which have not been well studied with VLBI. To the best of our knowledge, before this study there were 21 EGRET sources with

published VLBI proper motion measurements (many of which were not of high reliability (VC94)), leaving 30 EGRET sources which had not been studied with VLBI at multiple epochs. Some of these sources had been imaged or had had a VLBI intensity measurement made, but proper motion studies had not been published. The study of which this paper is a part has attempted to examine as many EGRET sources as possible which had not been previously well observed with VLBI, using the geodetic VLBI database of the Washington VLBI correlator located at the U.S. Naval Observatory (USNO). Reports have already been published of the measurement of superluminal motion in the quasar 1611+343 (Piner & Kingham 1997a, hereafter Paper I) and the measurement of a more standard superluminal velocity for the quasar 1156+295 (Piner & Kingham 1997b, hereafter Paper II), which had previously had a much larger measured superluminal velocity than any other source (McHardy et al. 1993, 1990). Detailed observations of three more sources are presented in this paper.

A study such as this has several potential benefits. It is important to understand why some of the sources sharing the common characteristics of EGRET blazars have not been detected in γ -rays. One possible reason is that the γ -ray emission may be more narrowly beamed than the radio emission (von Montigny et al. 1995b). Other possible reasons include intrinsic differences between the sources and long timescale variability of the γ -ray emission. VLBI measurements of such things as apparent superluminal motion can provide information on important quantities such as the angle of the jet to the line-of-sight, and can help to address this question. High-resolution VLBI observations can also potentially discern any effects of γ -ray flares on the jet structure.

This study also demonstrates the usefulness of archival geodetic VLBI data for astrophysics. Several authors have used geodetic VLBI data for astrophysical purposes. All imageable sources in a single geodetic experiment were imaged by Charlot (1990), and geodetic VLBI images have been presented in papers on the individual sources 0528+134 (Krichbaum et al. 1995, Pohl et al. 1995), OJ287 (Vicente, Charlot, & Sol 1996), 4C 39.25 (Alberdi et al. 1993; Fey, Eubanks, & Kingham 1997), 3C273 (Charlot 1993), 3C345 (Tang, Rönnäng, & Bååth 1989), and BL Lac (Tateyama et al. 1998). Schalinski et al. (1993) and Britzen et al. (1994) discussed a large-scale project to image many geodetic VLBI sources over many experiments. The study of which this paper is a part has a similar large-scale scope, with over one hundred images of six EGRET sources having been studied in detail (Piner 1998). Using archival geodetic VLBI data has several advantages. Many sources are observed very frequently, allowing for excellent time sampling. The archive extends back to 1986, allowing for an approximate ten-year time baseline for most sources. Many of these sources were not observed by the astronomical VLBI community until after their announcement as EGRET sources in at least 1991. We discuss the selection of the

individual sources studied in this paper in § 2, the archived geodetic VLBI observations in § 3, the motions of the individual jet components in § 4, and astrophysical implications of these results in § 5. We use $H_0 = 100h \text{ km s}^{-1} \text{ Mpc}^{-1}$, $q_0=0.5$, and the flux $S \propto \nu^{+\alpha}$ throughout the paper.

2. Selection of Individual Sources

For this study, we wished to find EGRET sources which had many good observations in the USNO geodetic VLBI database and had not had VLBI proper motion measurements published. For the list of EGRET sources, we used the 43 strong detections of AGNs given in the second EGRET catalog (Thompson et al. 1995) and the catalog supplement (Thompson et al. 1996). We also included four sources — 3C66A, CTA 26, 1622-297, and 2155-304 — for which new results gave significant enough detections that there was little doubt they would be included as strong detections in future lists (Hartman 1996, private communication). These four sources are indeed included, along with four other new sources, in the recent list in Mukherjee et al. (1997).

Observations of 700 galactic and extragalactic sources are included in the USNO geodetic VLBI database from the beginning of the program in 1986 until 1996 November. Of the 47 EGRET sources considered, 39 had at least one observation in the database. Of these, 26 had at least one observation with the necessary (u, v) plane coverage to make an image, and 20 of these had been observed often enough and well enough to produce a series of images. Nine of these 20 sources already had reliable VLBI proper motion measurements published. The remaining 11 sources were 0202+149, 0208-512, 0235+164, CTA 26, 0537-441, 1156+295, 1510-089, 1606+106, 1611+343, 1622-253, and 1739+522. Two of these sources, 0208-512 and 0537-441, are being studied by Tingay et al. (1996), and we have already presented results on 1611+343 and 1156+295 in Papers I and II respectively. Of the remaining seven sources, we present detailed time series of 0202+149, CTA 26, and 1606+106 in this paper, and we have also produced some images of 0235+164, 1622-253, and 1739+522.

3. Observations

The VLBI observations used in this paper are from archived geodetic Mark III VLBI observations processed at the Washington VLBI Correlator Facility located at the U.S. Naval Observatory (USNO). The background details of this archival data and the reduction

techniques are described in Paper I. As discussed in Paper I, some images have been formed by combining data from several geodetic VLBI experiments close together in time. This can be done as long as there is negligible change in the observable source structure over the time span of the summed observations, which is true for all observations that were combined for this paper. When experiments were combined, the AIPS task DBCON was used to combine them as separate subarrays.

A total of 40 different antennas were used among all of the imaged observations presented in this paper, with a maximum of 11 being used for a single experiment. The individual geodetic VLBI experiments used to image 0202+149, CTA 26, and 1606+106 are listed in Table 1. When two or more experiments are listed at the same epoch, then these experiments were combined to produce an image at this epoch. When this was done the time coordinate used for that epoch was defined to be the average of the times of the individual observations, weighted by the number of measured visibilities per observation. We have observations over an approximate seven-year time baseline for 0202+149, a three-year time baseline for CTA 26, and a five-year time baseline for 1606+106. The source 0202+149 was imaged at 11 epochs at both 8 and 2 GHz, for a total of 22 images of this source. Similarly, 16 and 24 images were produced of CTA 26 and 1606+106 respectively. A total of 60 geodetic VLBI experiments were analyzed to produce the 62 images of these three sources.

In addition to the geodetic VLBI images, we have also used some VLBA images made as part of a study of the Radio Reference Frame (Johnston et al. 1995). These images are also at 8 and 2 GHz, with some additional images at 15 GHz. The images are courtesy of Fey (1996, 1997, private communications), but we performed the model fitting of the images independently. VLBA observations of other Radio Reference Frame sources are presented by Fey, Clegg, & Fomalont (1996) and Fey & Charlot (1997). A list of the VLBA observations used in this paper is given in Table 2. In general, the VLBA images have lower resolution due to their shorter baselines, but higher dynamic range than the geodetic VLBI images. Thus they can serve as useful consistency checks on the reality of fainter components but do not significantly improve the proper motion measurements.

3.1. Images

Figures 1 to 6 show time-series mosaics of some of the geodetic VLBI images, at 2 and 8 GHz, of 0202+149, CTA 26, and 1606+106. These figures display time along the y -axis and relative right ascension along the x -axis. The images are centered at the time coordinate at which the observation was made. The axis scalings have been chosen so that the images

Table 1: Observation Log of Geodetic VLBI Experiments Used

Exp# ^a	Name ^a	Date	Antennas ^b	0202+149		CTA 26		1606+106	
				Vis. ^c	Epoch ^d	Vis.	Epoch	Vis.	Epoch
5970	NAVY30	1989 Jul 23	Gi,Mp,N8,Ri	900	1
5971	NAVY31	1989 Aug 4	Gi,Ka,Mo,N8,Ri	600	1
5972	NAVY32	1989 Aug 7	Gi,Mp,N8,Ri	1700	1
5973	NAVY33	1989 Aug 17	Gi,Mp,N8,Ri	2000	1
5974	NAVY34	1989 Aug 24	Gi,Mp,N8,Ri	1800	1
6414	NAVY114	1991 Mar 6	Gi,Ka,N8,Ri	700	2
6415	NAV115	1991 Mar 11	Gi,Ka,N8,Ri	1200	2
6416	NAV116	1991 Mar 20	Gi,Ka,N8,Ri	900	2
6418	NAV118	1991 Apr 3	Gi,Ka,N8,Ri	1200	2
6419	NAV119	1991 Apr 9	Gi,Ka,N8,Ri	700	2
6555	GLOBAL	1991 Dec 17	Gi,Ha,Ho,Ka,Km,Se,We,Wt	6900	1
7982	POLAR-N1	1992 Jun 29	D1,Gi,Hy,Ks,Me,On	900	2
6554	PPM-S1	1992 Jul 15	D4,Gi,Ka,Ks,Sa,Se	2700	2
7992	GLOBAL	1992 Jul 21	Gi,Ha,Ho,Ka,Ks,Sa,Se,We,Wt	12300	2
5789	SN1BS9	1993 Apr 21	Br,Gi,Ka,La	2800	1
6191	NAEX31	1993 May 17	Gi,Ha,Ka,Ks,Ma,N8,Sa	2500	1
6214	NAEX32	1993 Jun 14	Al,Gi,Ha,Ho,Ka,Ko,Ks,Ma,N8,Sa	2400	3	1900	1
6573	NEOSB002	1993 Jun 24	Al,Gi,Ma,N8,Wt	800	3
6522	SATL-ALT	1993 Jun 25	D6,Ha,Hn,Sa,Sc	1100	3
6187	XASIA-2	1993 Jul 16	D4,Ha,Ho,Ks,Se,Wt	2700	3
8069	NAEX37	1993 Dec 6	Gi,Ha,Ho,Ko,Ks,Ma,N8,Wt	500	2
8024	NEOSB008	1993 Dec 9	Al,Ma,N8,On,Wt	900	2
6545	NAXG07	1994 Jan 10	Fo,Gi,Ko,Ma,N8,Wt	900	4
6591	NAXG08	1994 Jan 12	Al,Fo,Ha,Ho,Ka,Ks,Ma,N8	2300	4
6838	NEOSA038	1994 Jan 18	Br,Fo,Gi,Ko,Mk,N8,Sc,Wt	1800	2	1500	4
6905	PPMS2	1994 Mar 16	D4,Gi,Km,Ko,Se,Ur	1200	5
6931	NEOSB011	1994 Mar 24	Gi,Ma,N8,On,Wt	2100	5
6933	NEOSB013	1994 May 12	Al,Gi,Ma,N8,On,Wt	2100	5
6936	NEOSB016	1994 Sep 1	Al,Gi,Ma,N8,On,Wt,Y1	1900	3	2400	6
6937	NEOSB017	1994 Sep 8	Al,Gi,Ma,N8,On,Wt,Y1	1700	3	2300	6
6875	NEOSA075	1994 Oct 4	Fo,Gi,Ko,N8,Ny,Wt	2200	6
6938	NEOSB018	1994 Oct 5	Al,Gi,Ma,N8,On,Wt,Y1	2200	3	2800	6
6939	NEOSB019	1994 Oct 6	Al,Gi,Ma,N8,On,Wt,Y1	1100	3	3700	6
6885	NEOSA085	1994 Dec 13	Fo,Gi,Ko,N8,Ny,Wt	2400	7
6020	RDGTR1	1995 Jan 23	Cr,Fo,Ha,Ho,Ma,Mk,N8,Pt,Sa,Sc	4100	5
6891	NA091	1995 Jan 24	Fo,Gi,Ko,N8,Wt	1700	7
6534	RDNAP2	1995 Feb 1	Al,Br,Nl,Ov,We	800	4
6541	GTRF2	1995 Mar 6	Cr,D4,Gi,Km,Ko,Ny,We,Wt	2300	8
6629	PPMS1	1995 Mar 23	D4,Gi,Ho,Km,Ko,Se	900	5
6633	RDTPC1	1995 Apr 20	Br,Kp,Ks,Mk,Ov,Se,Ur	700	5
6909	NAEXS6	1995 Jun 14	Al,Gi,Mi,N8,Ny,Wt	500	6
6636	RDGTR3	1995 Jul 24	D6,Gi,Ha,Ho,Ko,Kp,Ks,Nt,Sa,Y1	3800	7
6780	GTRF4	1995 Aug 16	D6,Fo,Gi,Ha,Ho,Ko,Me,On,Sa,We,Y1	4200	9
6792	RDC95A	1995 Aug 23	Gi,Ko,Ny,On,We,Wt	1200	9
6990	RDC95B	1995 Aug 24	Gi,Ko,Ny,On,We,Wt	1300	9
6991	RDC95C	1995 Aug 25	Gi,Ko,Ny,On,We,Wt	800	9
6992	RDC95D	1995 Aug 26	Gi,Ko,Ny,On,We,Wt	1300	9
7080	NAEX46	1995 Oct 11	Al,Gi,Mi,N2,N8,We,Y1	1600	6
8129	NA129	1995 Oct 17	Fo,Gi,Ko,Mk,N2,Nl,Wt	4300	8	1300	6	1900	10
8132	NA132	1995 Nov 7	Fo,Ko,Mi,N2,Wt	1100	6
7311	RDSATL	1996 Mar 11	D6,Fo,Ha,Hn,Sc	600	7
7312	RDTPC	1996 Mar 11	Br,Gi,Ks,Mk,Ov	700	7	1800	11
8152	NA152	1996 Mar 26	Fo,Gi,Ko,N2,Ny,Wt	900	9

Table 1 (cont.): Observation Log of Geodetic VLBI Experiments Used

Exp# ^a	Name ^a	Date	Antennas ^b	0202+149		CTA 26		1606+106	
				Vis. ^c	Epoch ^d	Vis.	Epoch	Vis.	Epoch
7313	WPAC	1996 Mar 27	D4,Gi,Ko,Ks,Se	1100	11
7316	GTRF10	1996 Apr 23	Cr,D1,Gi,Ha,Ho,Ks,Ma,Ny,We	3100	11
7321	NAXS10	1996 Apr 24	Al,Gi,Ko,N2,Ny,Wt	9500	10
7323	RDNAP1	1996 Jul 11	Al,Gi,Nl,We,Yl	1000	8	2300	12
7317	RDGT11	1996 Jul 22	Br,D6,Fo,Ha,Ho,Ks,Mk,Ny,Sc	2100	12
7328	RDNAP2	1996 Jul 22	Al,Gi,Nl,We,Yl	800	8	2300	12
8175	NA175	1996 Sep 3	Fo,Gi,Ko,N2,Ny,Wt	1300	11

^aExperiment number and name as it appears in experiment summary file.

^bAntenna names, locations, and sizes are as follows: Al = ALGOPARK; Algonquin, Ontario; 46 m — Br = BR-VLBA; Brewster, WA; 25 m — Cr = CRIMEA; Simeiz, Crimea, Ukraine; 22 m — D1 = DSS15; Goldstone, CA; 34 m — D4 = DSS45; Tidbinbilla, Australia; 34 m — D6 = DSS65; Madrid, Spain; 34 m — Fo = FORTLEZA; Fortaleza, Brazil; 14 m — Gi = GILCREEK; Fairbanks, AK; 26 m — Ha = HARTRAO; Hartebeesthoek, South Africa; 26 m — Hn = HN-VLBA; Hancock, NH; 25 m — Ho = HOBART26; Hobart, Tasmania; 26 m — Hy = HAYSTACK; Westford, MA; 37 m — Ka = KAUAI; Kauai, HI; 9 m — Km = KASHIM34, KASH34; Kashima, Japan; 34 m — Ko = KOKEE; Kauai, HI; 20 m — Kp = KP-VLBA; Kitt Peak, AZ; 25 m — Ks = KASHIMA; Kashima, Japan; 26 m — La = LA-VLBA; Los Alamos, NM; 25 m — Ma = MATERA; Matera, Italy; 20 m — Me = MEDICINA; Medicina, Italy; 32 m — Mi = MIAMI20; Perrine, FL; 20 m — Mk = MK-VLBA; Mauna Kea, HI; 25 m — Mo = MOJAVE12; Goldstone, CA; 12 m — Mp = MARPOINT; Maryland Point, MD; 26 m — N2 = NRAO20; Greenbank, WV; 20 m — N8 = NRAO85_3; Greenbank, WV; 26 m — Nl = NL-VLBA; North Liberty, IA; 25 m — Nt = NOTO; Noto, Sicily, Italy; 25 m — Ny = NYALES20; Ny Alesund, Norway; 20 m — On = ONSALA60; Onsala, Sweden; 20 m — Ov = OV-VLBA; Big Pine, CA; 25 m — Pt = PIETOWN; Pietown, NM; 25 m — Ri = RICHMOND; Perrine, FL; 18 m — Sa = SANTIA12; Santiago, Chile; 12 m — Sc = SC-VLBA; St. Croix, US Virgin Islands; 25 m — Se = SESHAN25; Shanghai, China; 25 m — Ur = URUMQI; Xinjiang, China; 25 m — We = WESTFORD; Westford, MA; 18 m — Wt = WETTZELL; Wettzell, Germany; 20 m — Yl = YLOW7296; Yellowknife, Northwest Territory; 10 m.

^cNumber of measured visibilities per IF, rounded to the nearest hundred. To get total number of visibilities multiply by 8 for 8 GHz or 6 for 2 GHz.

^dDuplicate epoch numbers indicate combined experiments.

Table 2: VLBA Radio Reference Frame Observations Used

Date	Sources	Frequencies		Epoch ^a
		(GHz)		
1995 Jul 24	CTA 26, 1606+106	2,8		F1
1995 Oct 2	CTA 26	2,8		F2
1995 Oct 17	0202+149, 1606+106	15		F3
1996 Apr 23	0202+149, 1606+106	2,8,15		F4

^aEpoch identification for comparison with geodetic VLBI epochs.

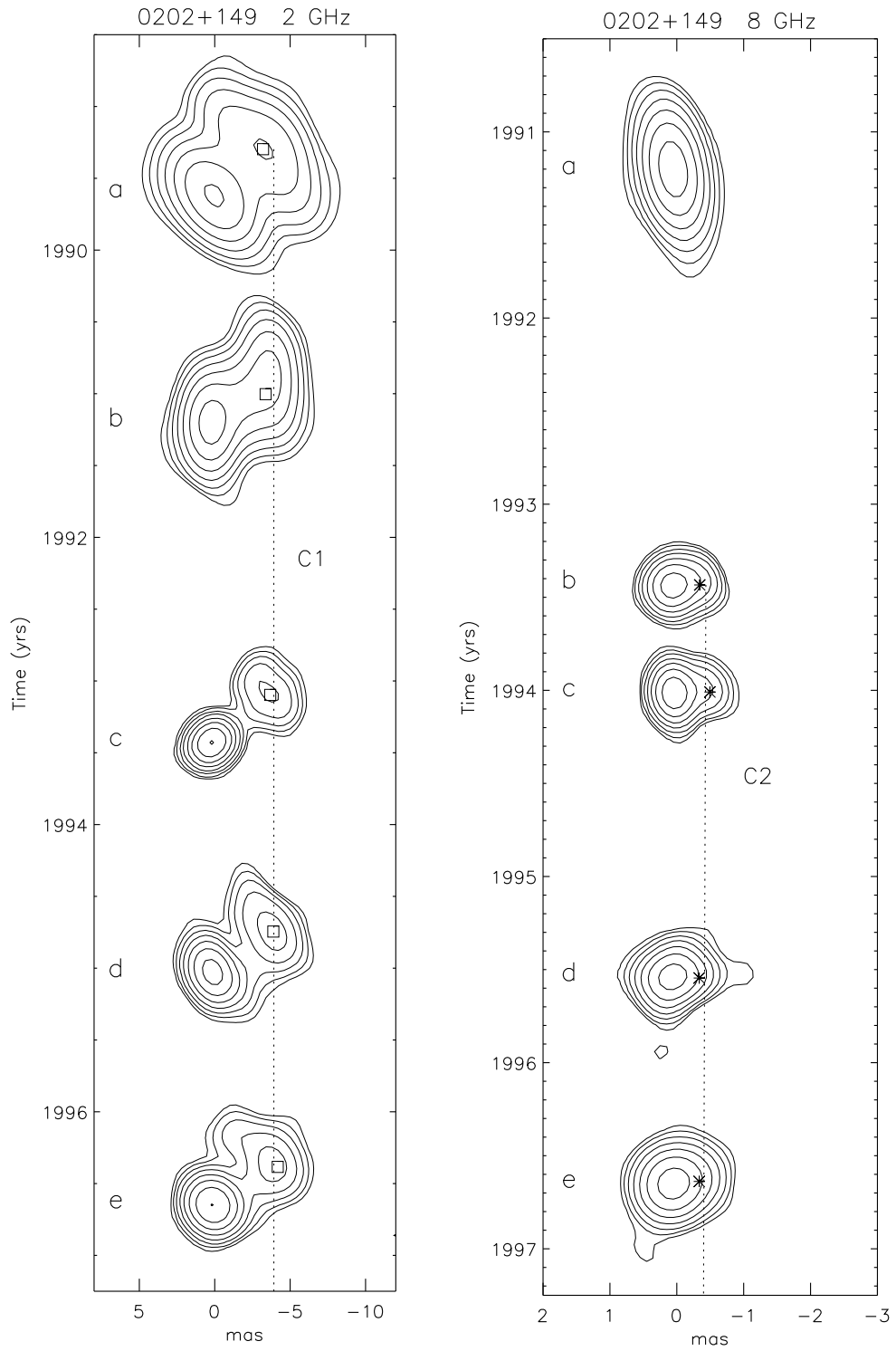
remain true to the original beam, and no distortion is introduced into the images. Because of space considerations, only about half of the VLBI images used in the analysis of these sources are shown in these figures. We believe we have selected those images which best demonstrate changes in source structure. Parameters of the displayed images are given in Table 3. The lowest contour for each image has been set equal to three times the rms noise in the image; however, noise contours have been suppressed in the time-series plots to avoid plotting a noise contour over an adjacent image.

The individual component positions as determined from model fitting (see § 3.2) are plotted on Figures 1 to 6, using various symbols. The dotted lines connecting these component positions represent the best fits to motion of the components at constant velocity, using measured positions from *all* epochs. Proper motion of components is easy to see by looking at these fits: A perfectly vertical line indicates a stationary component, and the more the line deviates from the vertical the faster the component is moving. Throughout the rest of this paper we follow the component numbering system of labeling the presumed core C0 and labeling the other components consecutively starting at C1, from the outermost component inward. Many of the differences in appearance from image to image within a series are due to the differences in the geodetic VLBI experiments. Experiments can vary drastically in both the lengths of the baselines and the sensitivities of the antennas. The geodetic VLBI experiments tend to have very long baselines which give high resolution; however, some experiments also have a dearth of short baselines, which can lead to an insensitivity to components which are farther out and more extended.

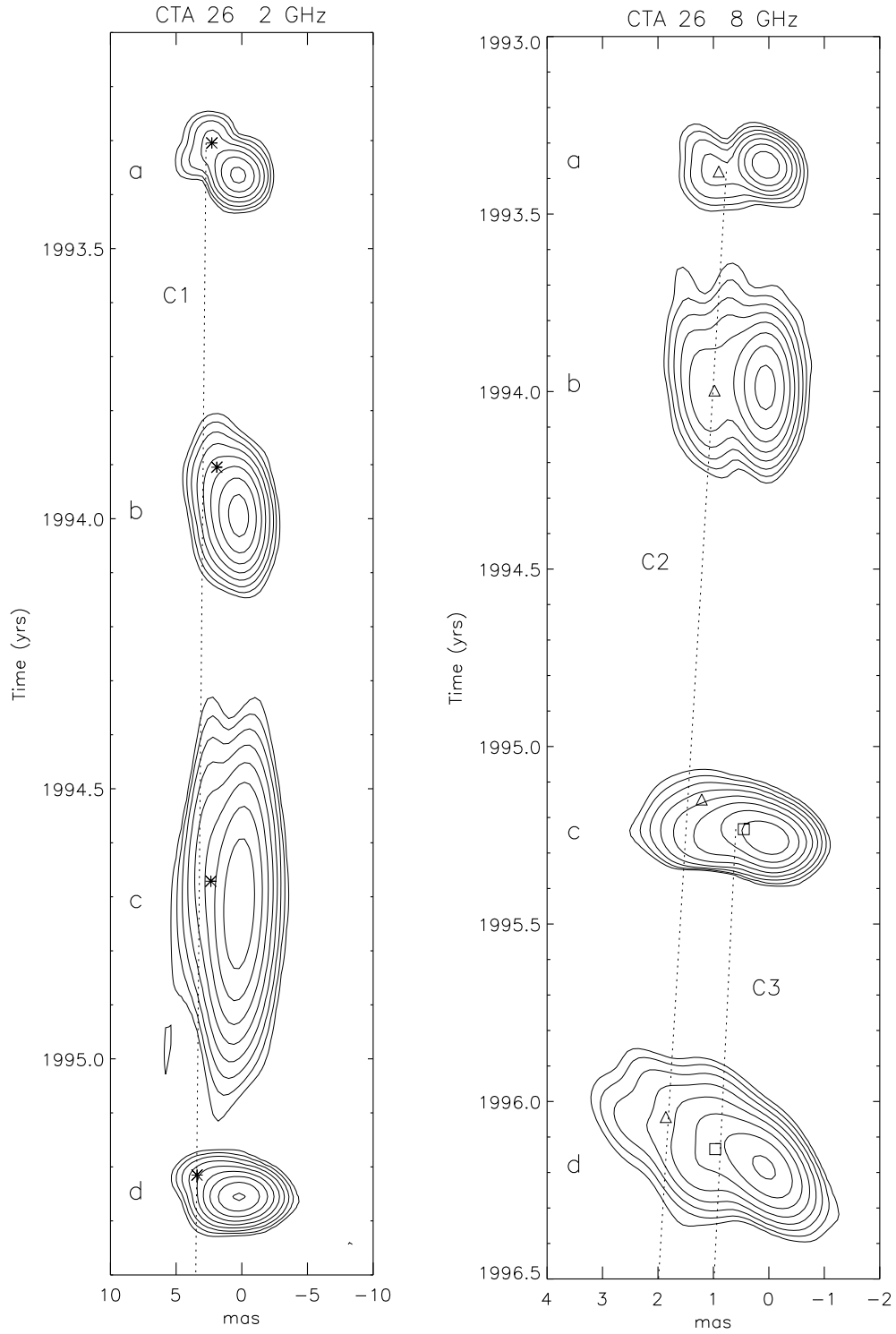
3.2. Model Fits

In order to quantify the positions and motions of the jet components, we fit Gaussian models to the observed visibilities for each epoch, using the MODELFIT procedure of the Caltech DIFMAP software package. The fitted components were either elliptical Gaussians, circular Gaussians, or delta functions. Elliptical Gaussians were fit where possible; if the ellipses became very elongated (axial ratio less than 0.1), then two or more circular Gaussians were used instead. If the circular components became very small (less than a tenth of a beam), then a delta function was used. Table 4 lists the fluxes and positions of the major components of the best fitting model for each image. We have included model fits for all of the observations listed in Table 1, as well as for the VLBA images listed in Table 2.

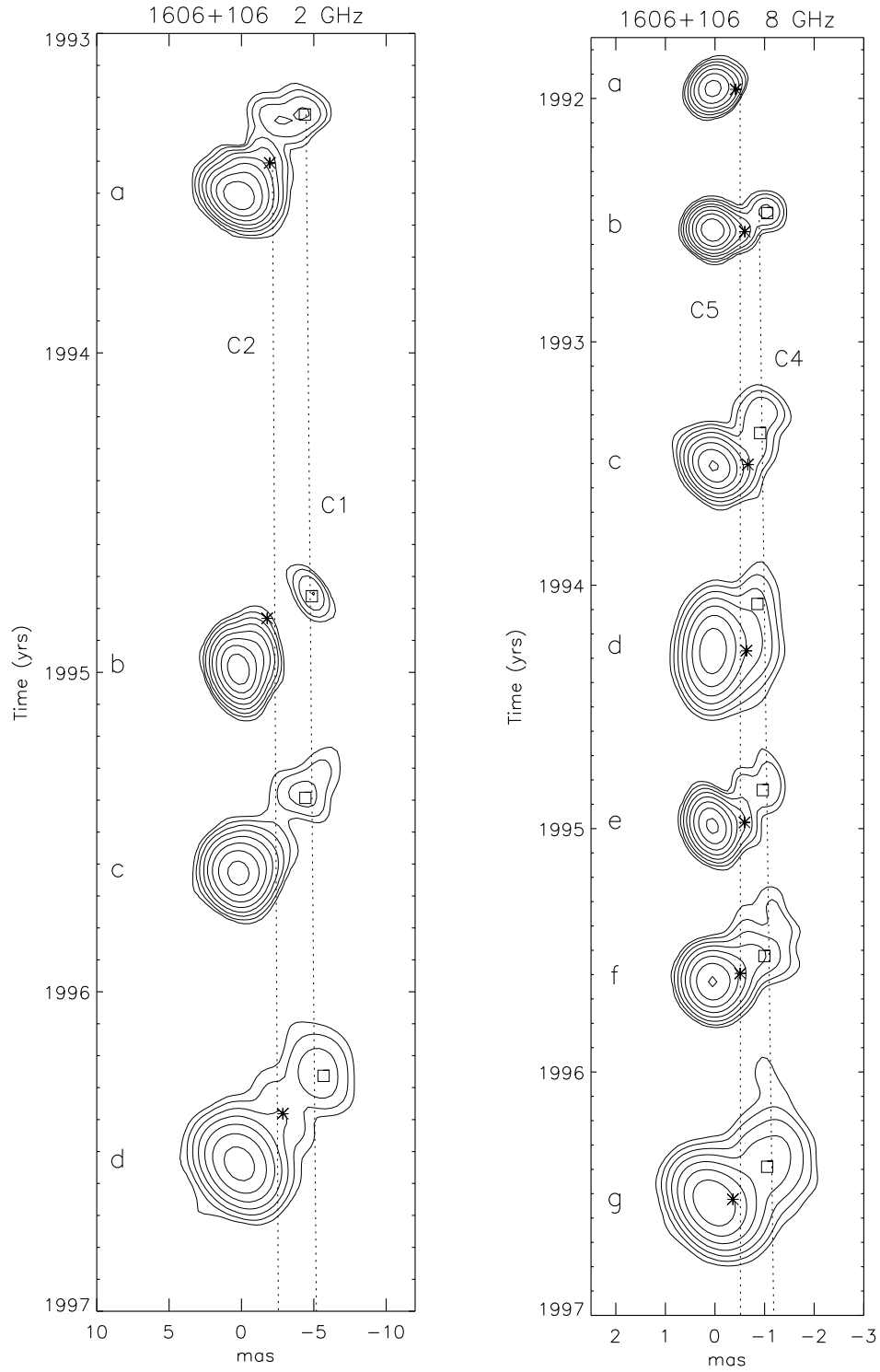
In Table 4, we have only included those components which we can unambiguously resolve. The lower resolution 2 GHz images usually see the core plus the inner 8 GHz



Figures 1 and 2: Time-series mosaics of 0202+149 images at 2 and 8 GHz respectively.



Figures 3 and 4: Time-series mosaics of CTA 26 images at 2 and 8 GHz respectively.



Figures 5 and 6: Time-series mosaics of 1606+106 images at 2 and 8 GHz respectively.

Table 3: Parameters of the Displayed Images

Source	Frequency (GHz)	Figure	Epoch ^a	Beam ^b	Contours (multiples of lowest contour)	Lowest Contour ^c (mJy beam ⁻¹)
0202+149	2	1a	1	4.56,2.70,31.8	1,2,4,8,16,32,64	17.0
		1b	2	3.89,2.23,3.2	1,2,4,8,16,32,64	11.5
		1c	3	1.92,1.68,-43.8	1,2,4,8,16,32,64,128	11.1
		1d	5	2.59,1.76,25.0	1,2,4,8,16,32,64	9.5
		1e	11	2.33,2.12,29.7	1,2,4,8,16,32,64,128	11.0
	8	2a	2	1.00,0.54,5.9	1,2,4,8,16,32,64	23.0
		2b	3	0.48,0.43,1.6	1,2,4,8,16,32,64	16.8
		2c	4	0.52,0.39,6.7	1,2,4,8,16,32,64	17.7
		2d	7	0.53,0.45,-60.5	1,2,4,8,16,32,64	16.1
		2e	11	0.61,0.57,14.9	1,2,4,8,16,32,64	15.6
		CTA 26	2	3a	1	2.07,1.84,26.3
3b	2	4.64,1.84,2.5		1,2,4,8,16,32,64,128	12.1	
3c	3	10.6,2.11,-2.8		1,2,4,8,16,32,64,128	8.7	
3d	5	2.69,1.95,-80.2		1,2,4,8,16,32,64,128,256	9.4	
8	4a	1		0.56,0.48,32.1	1,2,4,8,16,32,64	23.9
	4b	2		1.24,0.50,-0.5	1,2,4,8,16,32,64,128	9.0
	4c	5		0.70,0.53,-79.0	1,2,4,8,16,32,64,128	4.2
	4d	7		1.05,0.66,35.6	1,2,4,8,16,32,64,128	6.4
1606+106	2	5a	3	2.37,1.64,46.6	1,2,4,8,16,32,64,128	7.5
		5b	7	2.50,1.53,17.0	1,2,4,8,16,32,64,128	7.7
		5c	9	2.53,2.00,22.9	1,2,4,8,16,32,64,128	8.5
		5d	12	3.52,2.44,36.5	1,2,4,8,16,32,64	18.0
	8	6a	1	0.51,0.44,-31.6	1,2,4,8,16,32,64	12.3
		6b	2	0.48,0.45,55.8	1,2,4,8,16,32,64,128	7.1
		6c	3	0.64,0.45,39.8	1,2,4,8,16,32,64,128	7.8
		6d	5	1.07,0.59,-2.0	1,2,4,8,16,32,64	9.2
		6e	7	0.65,0.42,18.8	1,2,4,8,16,32,64,128	7.5
		6f	9	0.69,0.54,15.9	1,2,4,8,16,32,64,128	8.0
		6g	12	1.02,0.68,33.2	1,2,4,8,16,32,64	9.8

^aEpoch identification in Table 1.

^bNumbers given for the beam are the FWHMs of the major and minor axes in mas, and the position angle of the major axis in degrees.

^cThe lowest contour is set to be three times the rms noise in the image.

Table 4: Gaussian Models

Source	Epoch ^a	Component	Frequency (GHz)	S^b (Jy)	r^c (mas)	σ_r^d (mas)	PA ^c (deg)	σ_{PA}^d (deg)	a^e (mas)	b/a	Φ^f (deg)		
0202+149	1	C0	8	1.37	0.15	1.00	...		
			2	1.10		
	2	C1	2	0.98	4.58	0.28	-44.8	9.3	4.26	0.42	44.6		
		C0	8	2.52	0.51	0.19	19.8		
	3	C1	2	0.58	4.72	0.28	-54.9	7.1	1.18	1.00	...		
		C0	8	1.64	0.16	0.13	-53.0		
	4	C0	C2	8	0.46	0.38	0.07	-80.6	11.9	
			C1	2	0.59	4.97	0.19	-47.9	3.2	2.53	0.80	44.5	
			C0	8	2.07	0.12	0.58	-36.7	
	5	C0	C2	8	0.36	0.49	0.06	-82.4	10.0	
			C1	2	0.40	4.90	0.17	-57.4	3.3	1.94	0.16	-26.3	
			C0	8	2.04	0.29	0.56	-25.9	
	6	C2	C1	2	0.62	4.78	0.18	-53.2	5.1	2.98	0.45	39.4	
			C0	8	1.85	0.45	0.59	-1.1	
			C2	8	0.31	0.58	0.17	-58.6	17.0	
	7	C1	C0	2	0.77	4.31	0.40	-51.8	7.3	3.73	0.68	-22.1	
			C0	8	1.79	0.31	0.62	-11.9	
			C2	8	0.21	0.37	0.09	-84.9	11.8	
	8	C1	C0	2	0.34	4.89	0.21	-60.2	3.0	1.55	0.83	-48.5	
			C0	8	2.07	0.24	0.53	-62.8	
			C2	8	0.15	0.49	0.08	-80.5	13.9	
	F3	C0	C1	8	0.23	4.82	0.14	-48.5	2.0	2.48	0.22	55.0	
			C1	2	0.53	4.91	0.21	-53.0	5.3	2.74	0.54	22.3	
			C0	15	1.87	0.34	0.17	-19.7	
	9	C2	C1	15	0.26	0.34	0.12	-79.6	29.5	0.39	1.00	...	
			C1	15	0.21	4.99	0.17	-53.8	3.4	2.42	0.52	40.4	
			C0	8	1.44	
	F4	C0	C2	8	0.37	0.34	0.08	-63.6	20.0	0.42	1.00	...	
			C1	2	0.37	4.53	0.16	-56.5	5.5	2.42	0.58	30.5	
			C0	15	1.52	0.27	0.23	-26.9	
	10	C0	C2	8	1.66	
			C2	15	0.28	0.39	0.15	-50.9	21.1	0.64	0.29	76.8	
			C2	8	0.21	0.50	0.28	-65.9	32.7	0.24	1.00	...	
			C1	15	0.21	5.12	0.22	-54.0	2.6	2.41	0.41	36.2	
			C1	8	0.25	5.14	0.48	-53.8	4.6	2.10	0.48	30.3	
			C1	2	0.41	4.49	0.67	-57.4	13.1	2.55	0.53	-2.1	
	11	C0	C2	8	1.41	0.24	0.53	-34.6	
			C2	8	0.13	0.54	0.15	-68.4	18.7	
			C1	8	0.12	5.11	0.28	-52.5	2.5	1.76	0.38	20.0	
	11	C1	C2	2	0.24	4.88	0.40	-55.0	7.1	1.11	1.00	...	
			C0	8	1.50	0.28	0.25	-52.7	
			C2	8	0.30	0.38	0.09	-76.6	15.1	0.27	1.00	...	
	CTA 26	1	C0	C1	2	0.34	4.93	0.21	-56.7	4.5	2.10	0.37	17.9
				C2	8	0.78	0.90	0.13	94.4	8.6	0.85	0.60	45.4
				C1	2	0.31	3.67	0.51	45.3	7.2
		2	C0	C2	8	1.81	0.34	0.54	63.4
				C2	8	0.56	0.97	0.13	90.0	17.8	0.88	0.79	-3.9
				C1	2	0.16	4.41	1.07	27.7	8.3	1.04	1.00	...
3		C0	C1	8	1.16	
			C3	8	0.66	0.48	0.04	90.3	20.8	
			C2	8	0.28	1.22	0.29	108.2	29.1	

Table 4 (cont.): Gaussian Models

Source	Epoch ^a	Component	Frequency (GHz)	S^b (Jy)	r^c (mas)	σ_r^d (mas)	PA ^c (deg)	σ_{PA}^d (deg)	a^e (mas)	b/a	Φ^f (deg)
1606+106	4	C1	2	0.26	3.65	1.36	58.3	32.6
		C0	8	0.99
		C3	8	0.79	0.69	0.08	92.1	27.1
	5	C2	8	0.22	1.74	0.42	76.1	38.7
		C1	2	0.19	4.70	4.03	36.5	35.1	5.01	1.00	...
		C0	8	0.94	0.21	1.00	...
	F1	C3	8	0.64	0.62	0.04	64.7	3.4	0.42	1.00	...
		C2	8	0.17	1.54	0.16	58.9	5.7	0.28	1.00	...
		C1	2	0.08	4.27	0.61	63.7	7.5
	F2	C0	8	0.93
		C3	8	0.70	0.67	0.08	61.2	10.1	0.85	0.20	-82.7
		C2	8	0.23	1.68	0.30	69.7	16.5	1.83	0.44	22.2
	6	C1	2	0.07	6.12	1.23	61.4	15.6	3.79	1.00	...
		C0	8	1.18
		C3	8	0.63	0.79	0.08	66.5	9.6	0.92	0.60	-67.5
	7	C2	8	0.18	1.64	0.35	58.2	17.5	1.89	0.63	13.4
		C0	8	1.21	0.27	1.00	...
		C3	8	0.63	0.81	0.05	62.8	7.6	0.88	0.36	-85.7
	8	C2	8	0.13	1.95	0.21	58.5	12.4	0.68	1.00	...
		C0	8	1.07	0.52	0.51	51.0
		C3	8	0.53	1.03	0.06	67.9	2.8	1.02	0.52	-23.9
	1	C2	8	0.14	2.08	0.25	62.5	5.2	0.96	1.00	...
		C0	8	0.76
		C3	8	0.82	0.97	0.21	73.8	16.3	2.09	0.33	...
	2	C0	8	1.16	0.14	1.00	...
		C5	8	0.07	0.41	0.12	-85.6	16.8
		C0	8	1.85	0.15	0.90	82.7
	3	C5	8	0.08	0.60	0.12	-88.3	10.8
		C4	8	0.06	1.12	0.11	-69.7	5.9
		C0	8	1.37	0.31	0.68	-47.6
	4	C5	8	0.08	0.64	0.13	-83.6	13.1
		C4	8	0.07	1.12	0.11	-51.4	8.1	0.30	1.00	...
		C3	8	0.04	1.65	0.12	-36.6	5.5
	5	C2	2	0.16	3.22	0.41	-38.5	10.4	1.34	1.00	...
		C1	2	0.08	7.32	0.41	-37.2	4.6	1.31	1.00	...
		C0	8	0.91	0.18	0.60	-7.1
	6	C5	8	0.13	0.51	0.15	-58.8	27.5
		C0	8	1.01	0.27	0.73	-40.3
		C5	8	0.20	0.64	0.15	-84.6	22.6	0.63	1.00	...
	7	C4	8	0.03	1.31	0.23	-40.8	8.8
		C2	8	0.05	4.08	0.22	-45.7	3.0	0.44	1.00	...
		C0	8	1.16	0.15	0.27	-61.0
	8	C5	8	0.15	0.44	0.11	-79.0	19.8
		C4	8	0.06	1.10	0.12	-62.4	7.9	0.24	1.00	...
		C2	8	0.07	4.31	0.30	-36.0	3.3	0.39	1.00	...
	8	C0	8	1.32	0.24	0.54	-81.6
		C5	8	0.07	0.61	0.11	-78.4	14.9
		C4	8	0.10	1.23	0.11	-51.4	7.3	0.65	1.00	...
8	C3	8	0.02	1.91	0.14	-26.1	4.1	
	C2	2	0.02	4.14	0.53	-26.3	7.0	
	C1	2	0.06	7.18	0.45	-43.2	4.6	
8	C0	8	1.53	0.26	0.46	-46.8	
	C5	8	0.19	0.33	0.12	-83.6	23.1	

Table 4 (cont.): Gaussian Models

Source	Epoch ^a	Component	Frequency (GHz)	S^b (Jy)	r^c (mas)	σ_r^d (mas)	PA ^c (deg)	σ_{PA}^d (deg)	a^e (mas)	b/a	Φ^f (deg)
		C4	8	0.15	1.46	0.11	-50.2	5.8	0.39	1.00	...
	F1	C1	2	0.05	8.01	0.43	-37.4	3.7	1.46	1.00	...
		C3	8	0.03	2.35	0.44	-29.9	7.9	1.01	1.00	...
		C1	8	0.01	8.05	0.41	-39.1	2.6	1.68	0.96	62.6
	9		2	0.07	8.44	1.54	-35.5	8.6	4.52	0.33	-33.8
		C0	8	1.26	0.32	0.30	-69.8
		C5	8	0.11	0.55	0.14	-66.9	17.4	0.11	1.00	...
		C4	8	0.10	1.14	0.14	-60.5	8.5	0.65	0.10	59.5
		C3	8	0.05	1.97	0.15	-36.1	4.6	0.88	1.00	...
	10	C1	2	0.07	7.02	0.53	-39.7	4.9	1.10	1.00	...
		C0	8	0.74	0.22	1.00	...
		C5	8	0.12	0.58	0.21	-70.1	23.3
		C4	8	0.06	1.34	0.27	-45.6	8.1	0.22	1.00	...
		C1	2	0.08	7.55	1.22	-33.7	4.9	4.25	0.25	-87.8
	F3	C0	15	0.84	0.43	0.65	-68.4
		C5	15	0.11	0.59	0.23	-48.6	31.2	0.96	0.41	32.7
		C4	15	0.06	1.51	0.23	-46.0	13.1	0.57	1.00	...
	11	C0	8	1.23	0.31	0.37	-67.3
		C5	8	0.21	0.60	0.12	-61.9	14.6	0.40	0.18	27.9
		C4	8	0.12	1.48	0.12	-58.7	6.0
		C3	8	0.04	1.84	0.12	-42.2	4.8
		C2	2	0.05	3.05	0.49	-40.5	11.4
		C1	2	0.04	8.27	0.49	-44.2	4.2
	F4	C0	15	0.71	0.21	0.68	-63.7
		C5	15	0.19	0.50	0.17	-69.9	35.4	0.39	0.38	30.3
		C4	15	0.08	1.25	0.19	-57.0	15.5	0.67	1.00	...
		C3	15	0.03	1.97	0.23	-41.7	9.2	0.60	1.00	...
			8	0.03	2.08	0.57	-28.1	15.2	1.25	1.00	...
		C1	8	0.02	7.39	0.55	-31.7	4.5	2.39	1.00	...
			2	0.06	7.18	1.95	-32.3	16.5	4.50	0.37	18.6
	12	C0	8	1.08	0.18	0.73	-70.4
		C5	8	0.32	0.41	0.18	-70.2	31.3	0.33	1.00	...
		C4	8	0.21	1.34	0.17	-53.8	10.8	0.79	0.49	-41.8
		C3	8	0.03	2.09	0.17	-48.4	6.9
		C2	2	0.07	4.69	0.63	-37.6	10.4	0.81	1.00	...
		C1	2	0.15	8.49	0.62	-42.0	5.9	1.35	1.00	...

^aEpoch identification in Table 1 or Table 2.

^bFlux density in Janskys.

^c r and PA are the polar coordinates of the center of the component relative to the presumed core C0. Position angle is measured from north through east.

^d σ_r and σ_{PA} are the estimated errors in the component positions.

^e a and b are the FWHM of the major and minor axes of the Gaussian component.

^fPosition angle of the major axis measured from north through east.

components as only a single component. Since it is impossible to deconvolve these merged components and know how much flux is coming from each, we do not include these merged 2 GHz components in Table 4. In the model fits listed in Table 4 we have fixed the location of the presumed core to be at the origin and give positions for all other components relative to the core. For all three of these sources we have selected as the core the brightest compact component at the end of the extended jet structure. In all of these sources this component also has the flattest spectral index.

Determining accurate errors in the model-fit parameters is problematic. Formal methods for calculating the errors, such as that described by Biretta, Moore, & Cohen (1986), rely on varying a given parameter until the reduced χ^2 increases by a certain factor. This gives an estimate for the uncertainty in a parameter within that particular observation, but it does not take into account the differences in (u, v) plane coverage among observations in a series, which may cause differences in the model-fit parameters among observations which are much larger than the associated formal errors. Since geodetic VLBI observations can have drastically different antennas and (u, v) plane coverages, we might expect that this effect would dominate for a series of geodetic VLBI images. Indeed, we have used the method of Biretta, Moore, & Cohen (1986) to derive formal errors for the model-fit parameters of 1611+343 presented in Paper I, and it is obvious from the large scatter in the points that the formal errors are much too small.

The only way to derive an accurate estimate for the errors is to model fit a series of images made from observations with varying (u, v) plane coverages over a small enough time interval that the source structure does not change and note the scatter in the model-fit parameters. Many of the sources in the USNO database have observations close enough together in time that this can be done. Since we expect errors in the component positions to be proportional to the beam size, we express the errors as a fraction of the beam and note that for nearly simultaneous images of 1611+343 (Paper I), and 1606+106, the scatter in the model-fit component positions is about a quarter of a beam FWHM. We have accordingly used a quarter of a beam as the error in the position for most of the components, except for those noted below. For the beam size in a given direction we have used the maximum projection of the beam onto a line in that direction.

It is reasonable to suppose that model fitting will more accurately locate bright, compact components. From Condon (1997) it can be derived that the positional error should be proportional to $B^{-1/2}$, where B is the surface brightness of the component. We have accordingly used smaller error bars for the brighter, more compact components. We have used 1/6 of a beam for component C2 in 0202+149, and 1/16 of a beam for the very bright, very compact component C3 in CTA 26. The bright 2 GHz component C1 in

0202+149 is elongated perpendicular to the radial direction; we have used 1/10 of a beam for the radial error and 1/6 of a beam for the angular error. In all cases the observed scatter of the positions about the fitted lines agrees with the chosen error bars. For the fitted fluxes the calibration error must be added to the model fitting error. Since the calibration errors are relatively large for these geodetic VLBI experiments, the model-fit fluxes are in general not very accurate, except possibly for the very bright components.

4. Motion of Components

In this section we discuss the motions of the individual components in both radius and position angle. Two of the sources, CTA 26 and 1606+106, have components moving outward at apparent superluminal velocities, while the components in 0202+149 are clearly subluminal. We have calculated values for the apparent velocities by performing least-squares fits to the component distances from the cores as a function of time, using the model-fit positions and errors discussed in the preceding section. In all cases a linear fit was adequate, i.e. we have no significant detection of acceleration or deceleration of any of the components. When a component was detected at more than one frequency, we fit the positions measured at each frequency separately to avoid effects from frequency-dependent separation. We then took the weighted average of the velocities measured at the different frequencies to obtain a single value for the velocity. For all three of the sources discussed here, the velocities measured for the individual components are consistent with all components within the source having the same velocity.

Motion of the jet components in position angle is also discussed in this section. All position angle values are measured from north through east. Here we also present data on the motion of the components of 1156+295 in position angle, since only the outward motions of the 1156+295 components were discussed in Paper II. Curved jets on VLBI scales are a common feature of blazars, and we observe bent jets in the sources we have studied. In fact, we have highly significant detections of different position angles for different components for all five of the sources we have studied in detail. Whether or not individual components move in position angle, and whether or not they follow other components, must be examined on a case-by-case basis. This requires longer monitoring of individual components, and preferably waiting until a component reaches the same radial distance from the core previously occupied by an earlier component. For 1611+343 (Paper I), we found that components were located at different position angles, but that motion with constant position angle was adequate to fit individual component motions. We observed significantly different position angles for components at the same radial distance,

which ruled out motion of the components along identical curved paths.

4.1. 0202+149

The source 0202+149 is a flat-spectrum radio quasar with a redshift of 0.833 (Stickel et al. 1996). Bondi et al. (1996), Padrielli et al. (1986), and Romney et al. (1984) imaged this source with VLBI at three epochs (1980 February, 1981 October, and 1987 November) at 1.7 GHz as part of a campaign to study the structure of low-frequency variable sources. They found that the structure of 0202+149 was well fit by a model with two components separated by ≈ 3.4 milliarcseconds (mas) along a position angle of $\approx -71^\circ$. The separation of the components did not change significantly over the three epochs, although the low resolution of the observations does not allow the authors to place a very strict upper limit on the proper motion. They find that both components vary in flux, the southeastern component brightens, and the northwestern component fades over the three epochs. A 22 GHz VLBI observation by Moellenbrock et al. (1996) measured a brightness temperature for 0202+149 in excess of the inverse Compton limit for synchrotron radiation (10^{12} K), indicating the likelihood of relativistic beaming in this source.

The separations from the core as a function of time that we measure from our images are shown in Figures 7*a* and *b* for components C1 and C2 respectively. By taking the weighted average of the velocities found from separate fits to the 2, 8, and 15 GHz positions of C1, we calculate an outward velocity of $0.11 \pm 0.88 h^{-1}c$ for this component. Similarly, we measure a velocity of $-0.23 \pm 0.65 h^{-1}c$ for component C2. Both of these velocities are consistent with no motion, and the one-sigma upper limits are 0.99 and $0.42 h^{-1}c$ for C1 and C2 respectively. Since the measured positions are consistent with stationary components, we have plotted the best fits to constant separation from the core in Figures 7*a* and *b*. In Figure 7*a* the fitted separations are at successively greater distances from the core as the frequency increases. This frequency-dependent separation was also seen in 1156+295 (Paper II) and has been noted by other authors (e.g. Biretta, Moore, & Cohen 1986). It may be due to gradients in magnetic field and electron density, which cause the $\tau = 1$ surface to move progressively inward at higher frequencies. The frequency-dependent separation in Figure 7*b* appears to go in the wrong direction, although the error bars on the 15 GHz points are such that this separation is not significant.

The VLBI observations of 0202+149 at 1.7 GHz presented by Bondi et al. (1996) show a bright component about 3.4 mas from the core which can probably be identified with our component C1. Although their three measured positions are also consistent with the component having no motion, their measured separation is about 1.4 mas closer to the core

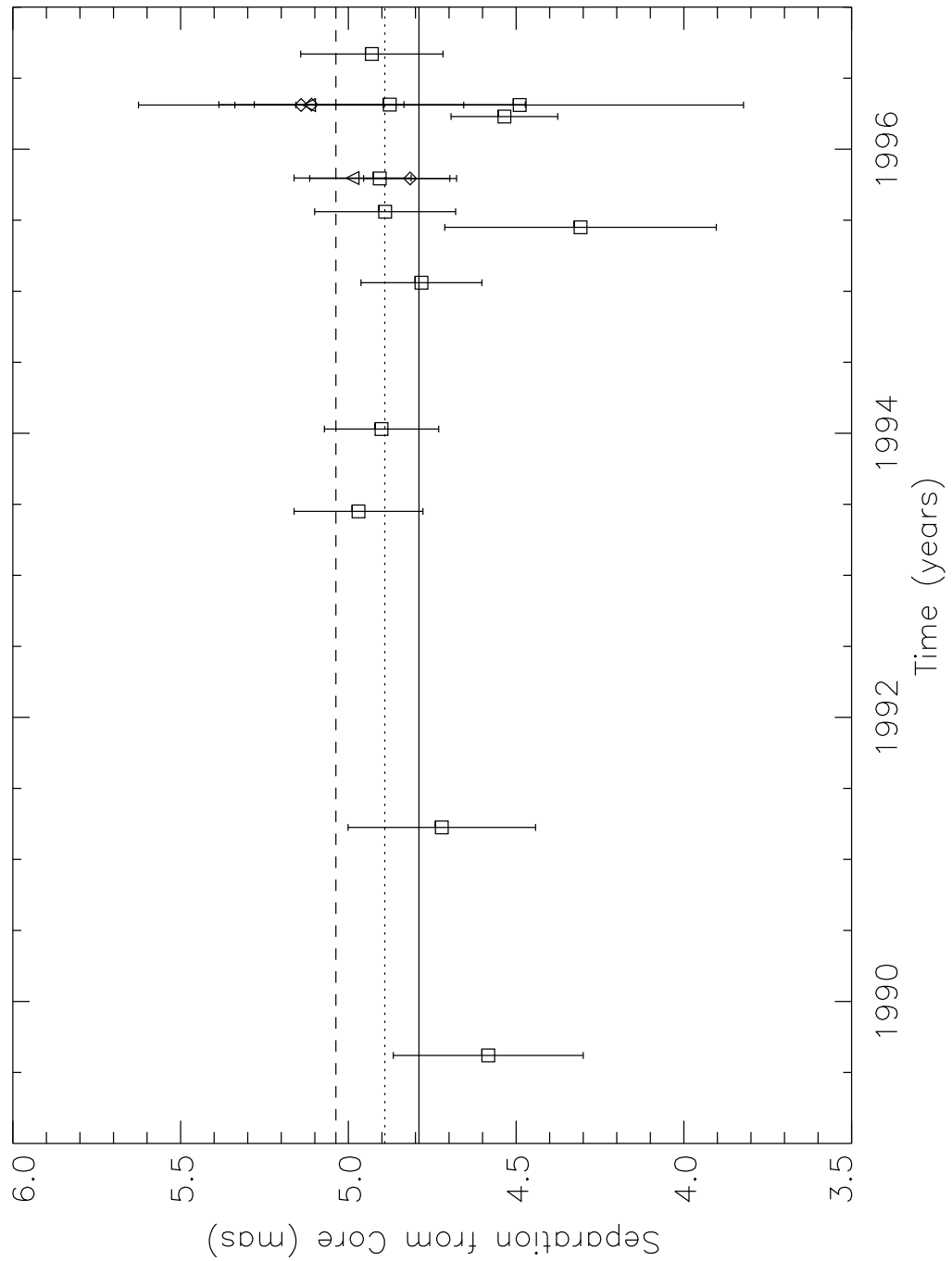


Figure 7a: Separation of component C1 in 0202+149. Squares represent the 2 GHz positions, diamonds 8 GHz, and triangles 15 GHz. The lines shown are the best fits to constant separation from the core. The solid line is the best fit to the 2 GHz positions, the dotted line to the 8 GHz positions, and the dashed line to the 15 GHz positions.

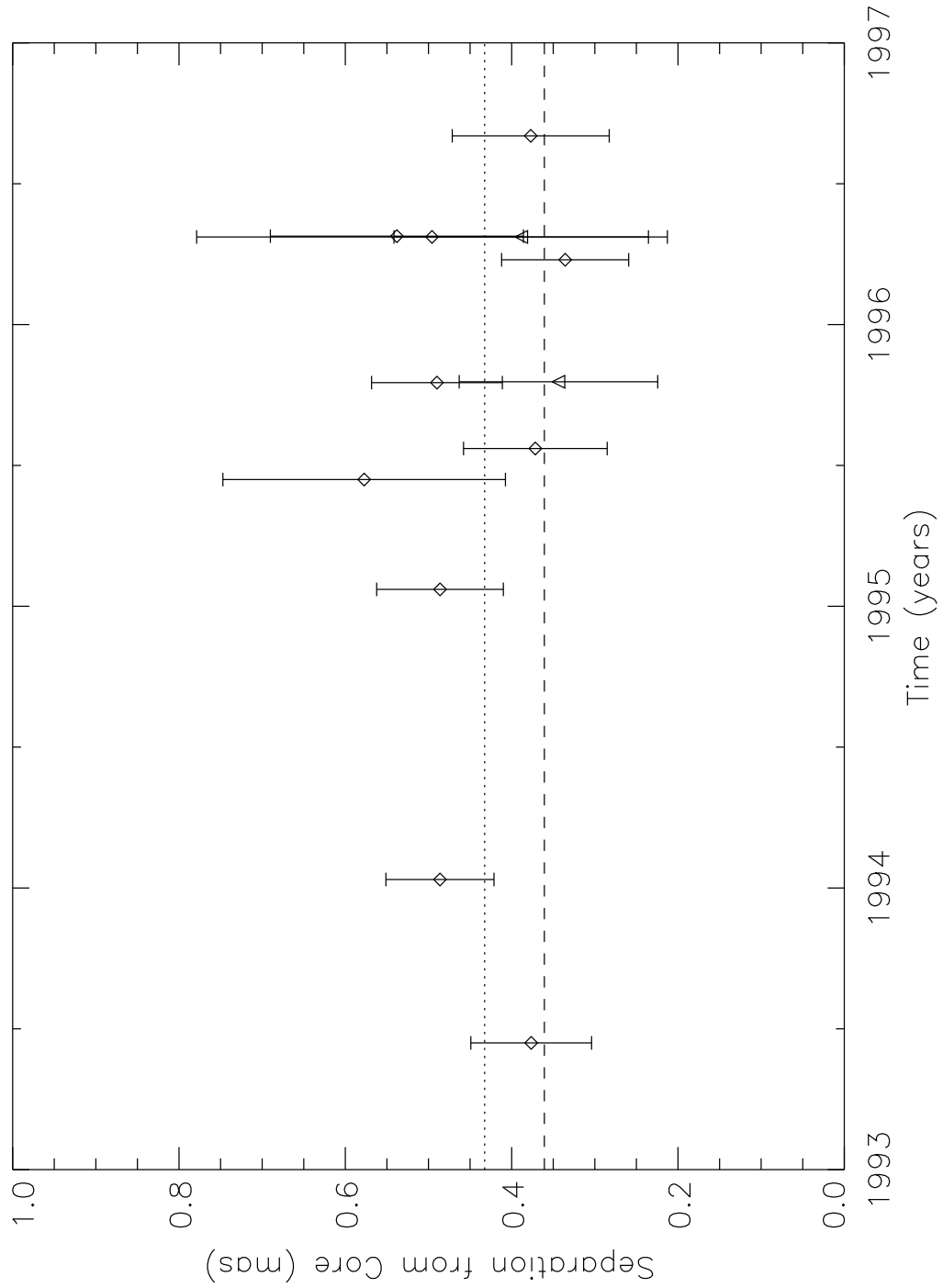


Figure 7b: Separation of component C2 in 0202+149. Diamonds represent the 8 GHz positions and triangles the 15 GHz positions. The lines shown are the best fits to constant separation from the core. The dotted line is the best fit to the 8 GHz positions, and the dashed line to the 15 GHz positions.

than ours. If a fit is done to the Bondi et al. (1996) positions which cover the time range 1980 to 1987, combined with our measured 2 GHz positions which cover the time range 1989 to 1996, then a slightly superluminal velocity of $1.8 \pm 0.5 h^{-1}c$ is obtained. However, this velocity comes entirely from the difference in separation between the Bondi et al. (1996) points and our points, and each set of measurements individually is consistent with no motion. We suspect that this velocity may arise from frequency-dependent separation combined with systematic differences between the two sets of observations, and we use only the velocity obtained from fits to our actual measured component positions.

Component C2 also appears to be stationary at 0.41 mas from the core, but this component is not present in the images from 1989 and 1991. Either this component really is moving outward, or it may represent a standing shock in the underlying flow which appeared in this location sometime between 1991 and 1993. If this component were moving at its 2σ upper limit proper motion of 0.04 mas yr^{-1} , then in 1991 it could have been only 0.33 mas from the core and may have been unresolved in these earlier images. The high 8 GHz core flux in the 1991 image may support this. If this is so, then the velocity of C2 would actually be around $1.0 h^{-1}c$.

The components in this source are stationary in position angle as well as in radius. However, they have different position angles from each other. The measured position angle of C1 is $-53.0 \pm 0.9^\circ$, and that of C2 is $-75.0 \pm 4.3^\circ$. The average position angle of C1 from the observations presented by Bondi et al. (1996) is -71° , with no error bars given for the position angles. Their error bars are likely to be quite large because of the large size and ellipticity of their beams. If the difference between the Bondi et al. (1996) C1 position angle and our C1 position angle is in fact significant, this would imply motion of C1 from a position angle close to that of C2 to its present position angle over the time between the Bondi et al. (1996) observations and the present. This would imply motion of C1 at close to its one-sigma upper limit velocity.

4.2. CTA 26

The quasar CTA 26 (0336-019) is a core-dominated flat-spectrum radio source at a redshift of 0.852 (Hewitt & Burbidge 1989). A 5 GHz VLBI image from Wehrle et al. (1992) shows a jet at a position angle of about 65° , roughly orthogonal to the VLA secondary. Relativistic beaming is indicated by the VLBI observations of Linfield et al. (1989), who measure a brightness temperature well in excess of the 10^{12} K inverse Compton limit.

Figures 8*a* and *b* show the outward motions that we measure for the components

of CTA 26. The motion of the outermost component C1 is shown in Figure 8*a*. This component was only detected at 2 GHz. The lower 2 GHz resolution, in combination with very elliptical beams at some epochs, has resulted in rather large errors in the position measurements for this component. These errors lead to a large error in the fitted velocity, which is $12.6 \pm 9.6 h^{-1}c$. This component fades over time and is not visible in the 2 GHz images after mid 1995.

The motions of the two components which we detected in the 8 GHz images, C2 and C3, are shown in Figure 8*b*. Component C2 was detected in the earliest image and continued to be visible over most of the covered time range, although it faded as time went on. Component C3 was first detected in late 1994 and was visible in all subsequent images. The measured outward velocities for these two components are $10.5 \pm 1.6 h^{-1}c$ for C2, and $8.3 \pm 1.0 h^{-1}c$ for C3. These measured velocities and standard errors are consistent with all three components moving at the weighted average velocity of $8.9 \pm 0.8 h^{-1}c$. This value is near the high end of the apparent velocity distribution for core-dominated quasars. This distribution appears to have a cutoff around speeds of $10 h^{-1}c$ (VC94); however, velocities between 8 and $10 h^{-1}c$ are not uncommon.

Figure 9 shows the measured separations and position angles of all components at all frequencies and all epochs for CTA 26. We plot r on a logarithmic scale to aid in display of both inner and outer components. Motion with constant position angle corresponds to motion along a horizontal line on this plot. The motion of C3 is well fit by motion at a constant position angle of $66.6 \pm 2.0^\circ$; however, we have a greater than 2σ detection of change in position angle for both C2 and C1. C2 decreases its position angle from about 100° to about 60° as it moves from 1 to 2 mas, while C1 increases its position angle with time. If C2 and C1 define a single path, evidently the components move toward lower position angles from radii around 1 mas to radii around 3 or 4 mas, at which time they curve back to higher position angles. Such oscillations in position angle are expected in the helical models which have been proposed to explain some curved jets (e.g. Hardee 1987). Although C2 and C1 may define a single path, it is evident that C3 has taken a different path out from the core than C2. C3 is at a lower position angle than C2 when C2 was at the same radius. If C3 continues moving along its present straight path, it will merge with the path defined by C2 at a radius of between 1 and 2 mas. Components which take different paths out from the core and later merge onto the same curved path have been seen in 3C345 (Zensus, Cohen, & Unwin 1995).

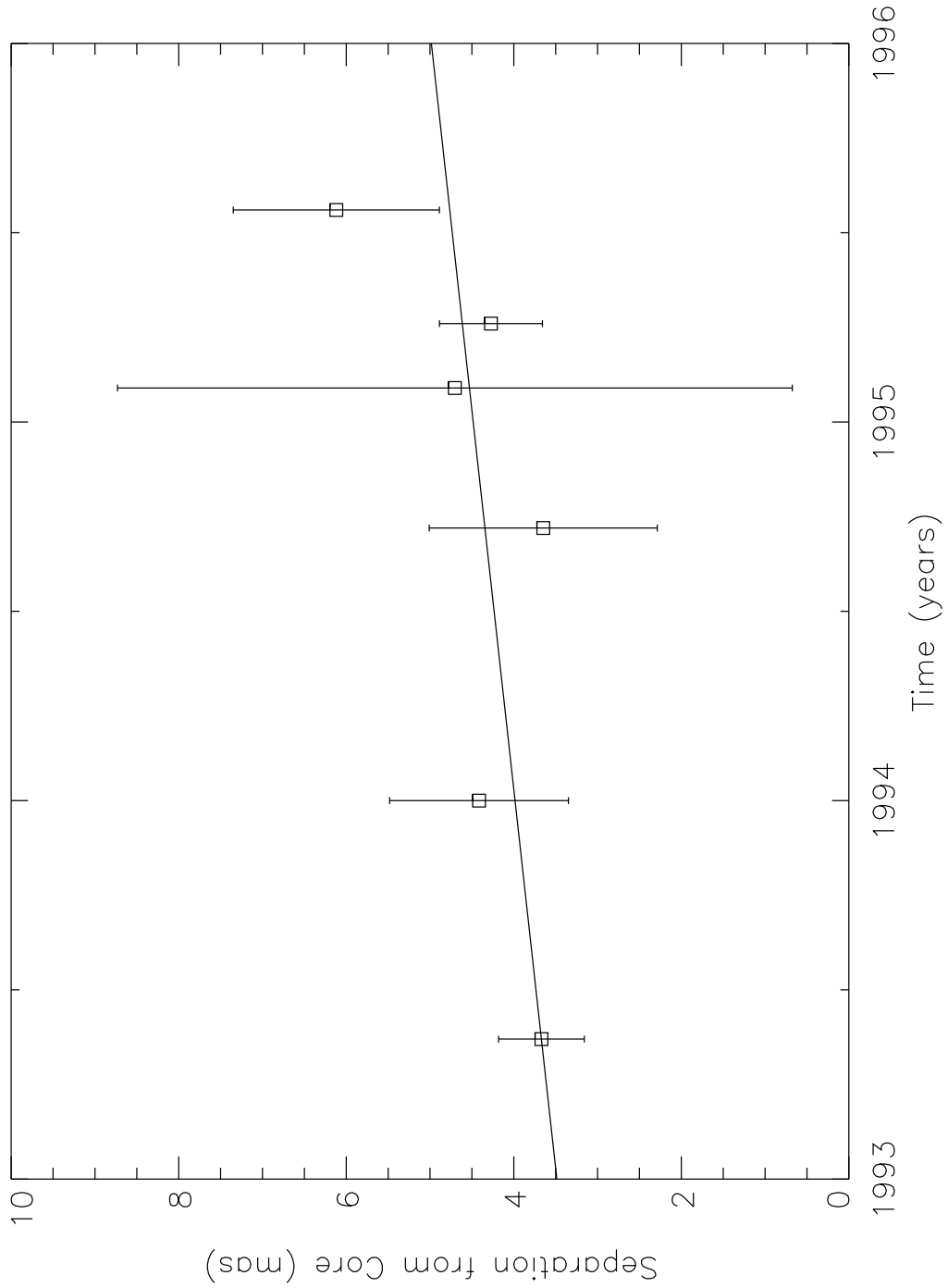


Figure 8a: Separation of component C1 in CTA 26. All measurements are at 2 GHz. The line is the best fit to motion with constant velocity.

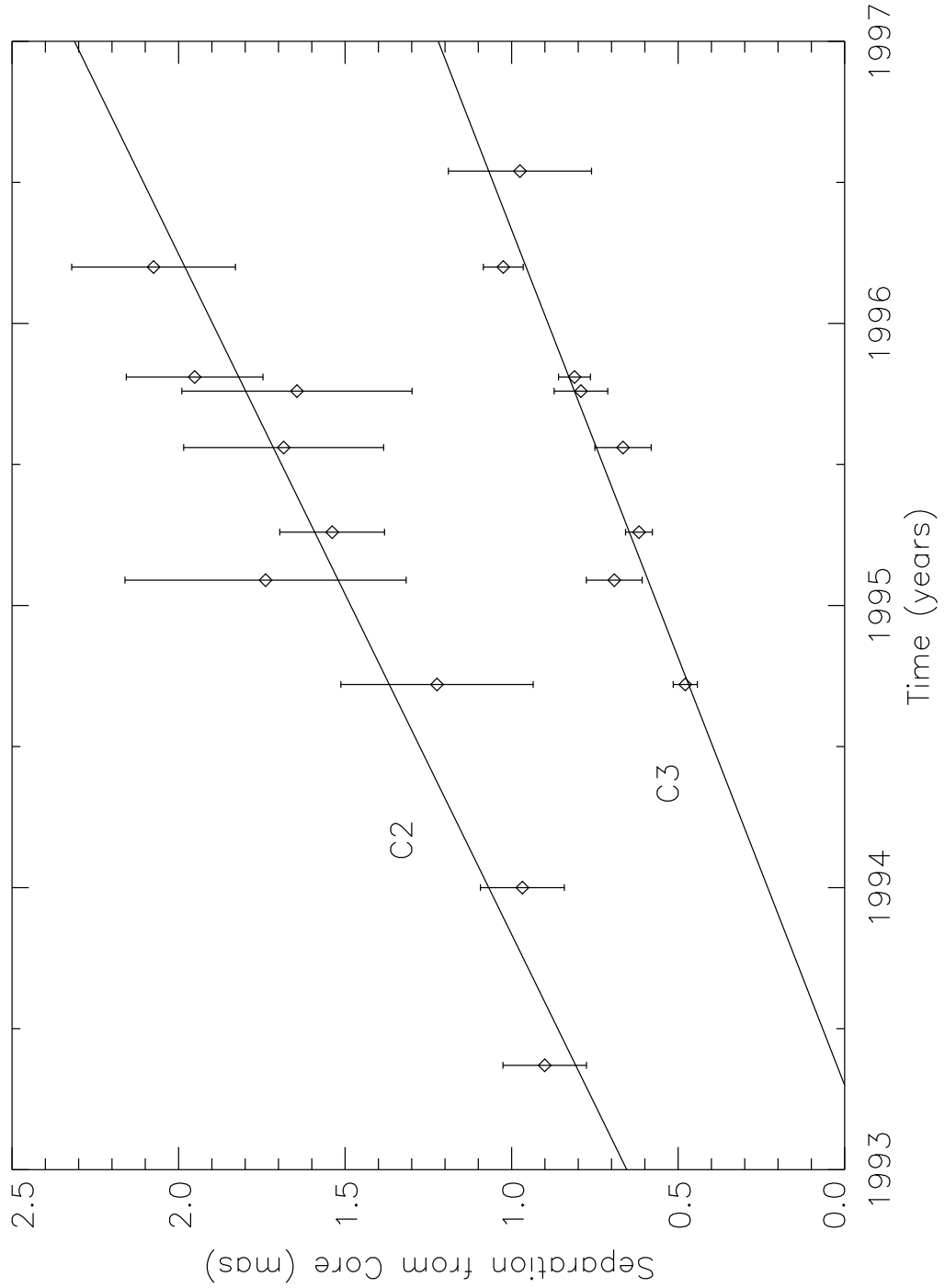


Figure 8b: Separation of components C2 and C3 in CTA 26. All measurements are at 8 GHz. The lines are the best fits to motion with constant velocity.

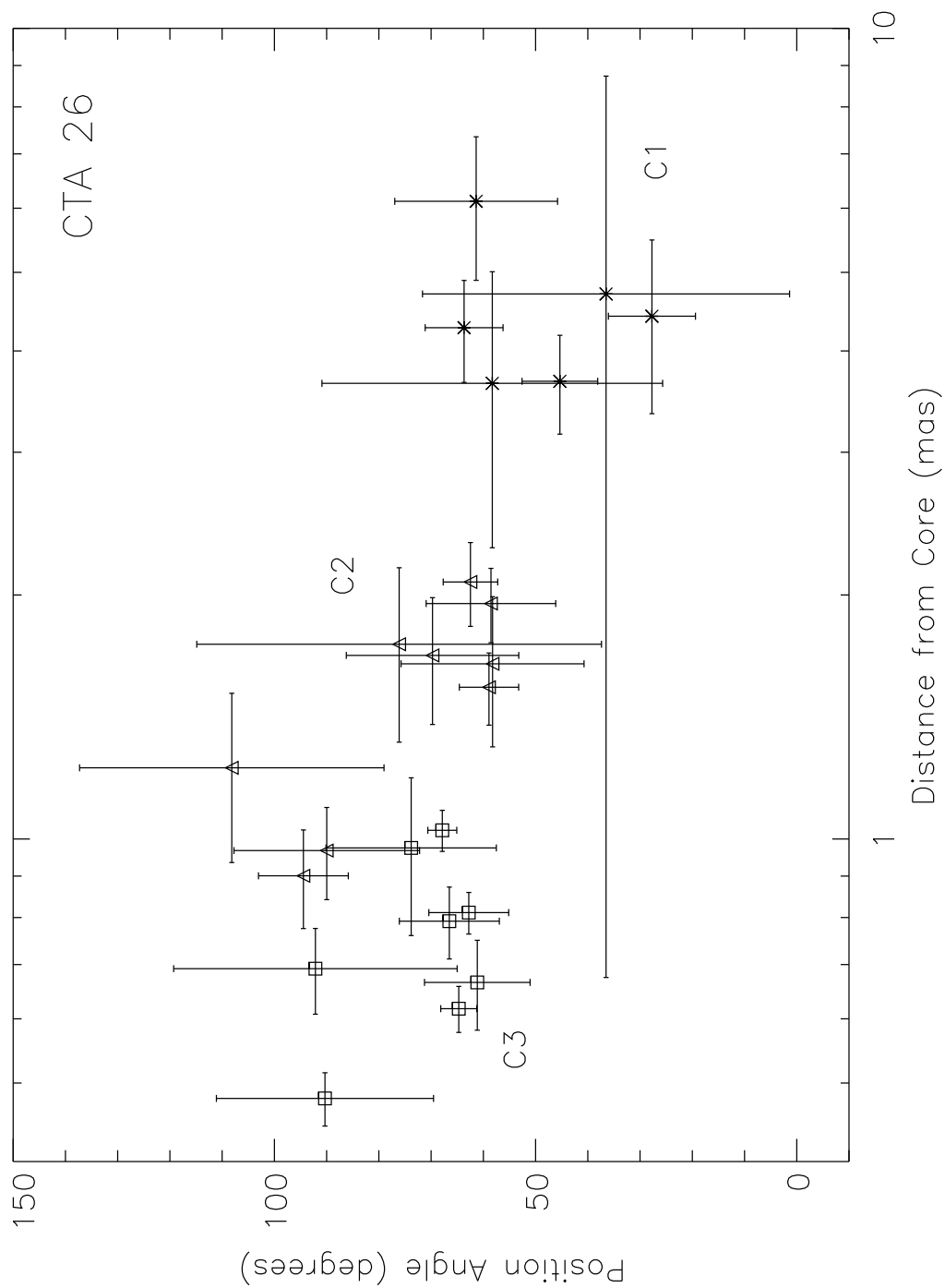


Figure 9: Measured positions of all components at all frequencies and all epochs for CTA 26. The x -axis shows the distance from the core on a logarithmic scale and the y -axis shows the position angle, measured from north through east. Asterisks show measured positions of C1, triangles C2, and squares C3.

4.3. 1156+295

The geodetic VLBI images and outward motions of the components of 1156+295 were discussed in Paper II. Here we discuss the motion of the components of this source in position angle. Figure 10 is the same as Figure 9 except it shows the component positions from 1156+295. The 2 GHz positions have been shifted out by 0.65 mas to correct for the observed frequency-dependent separation (Paper II). The motions of C1, C2, and C4 are well fit by constant position angles, which differ significantly from each other, of $36.0 \pm 2.6^\circ$, $15.2 \pm 1.9^\circ$, and $9.7 \pm 6.0^\circ$ respectively. We have a greater than 2σ detection of a change in position angle for C3, from 40° at 1 mas to -20° at 3 mas. Inspection of Figure 10 suggests a continuous path, consisting of oscillations in position angle, that the components could follow. The components could start at the core with a position angle of 0° and increase their position angle to about 20° at 1 mas, at which point they would turn and move toward lower position angles of around -20° at 3 mas. They could then curve back toward higher position angles, reaching a position angle of 35° at 10 mas. Whether or not such a path exists should become evident with continued monitoring. C4 has already reached the earliest C3 radius and is somewhat below that C3 position angle; however, the error bars on the earliest C3 point are large enough that this may not be significant. C3 has just now reached the radius of the earliest C2 point. If it is going to follow C2, it needs to start moving toward higher position angles soon.

4.4. 1606+106

The flat-spectrum radio quasar 1606+106 has a redshift of 1.23 (Stickel & Kühr 1994). This quasar was observed with VLBI at 5 GHz in a three-antenna experiment by Zensus, Porcas, & Pauliny-Toth (1984). It was well fit by a circular Gaussian of width 0.6 mas. At least three images of this source have been made from geodetic VLBI data by Britzen et al. (1994), although the images are not presented in that reference.

The components in the jet of 1606+106 are considerably fainter than the components in the other two sources studied here, so not all components are detected by us at all epochs. In general, our later observations of 1606+106 had superior sensitivity and (u, v) plane coverage, and were better able to detect the fainter components. Figure 11a shows the measured positions of the outer components, C1 and C2, from our images. These components were both mainly detected in the 2 GHz images, although there are some 8 GHz detections of each. The weighted average of the velocities measured at 2 and 8 GHz are 8.0 ± 5.9 and $6.1 \pm 6.0 h^{-1}c$ for C1 and C2 respectively, where the large error bars are the result of the lower 2 GHz resolution.

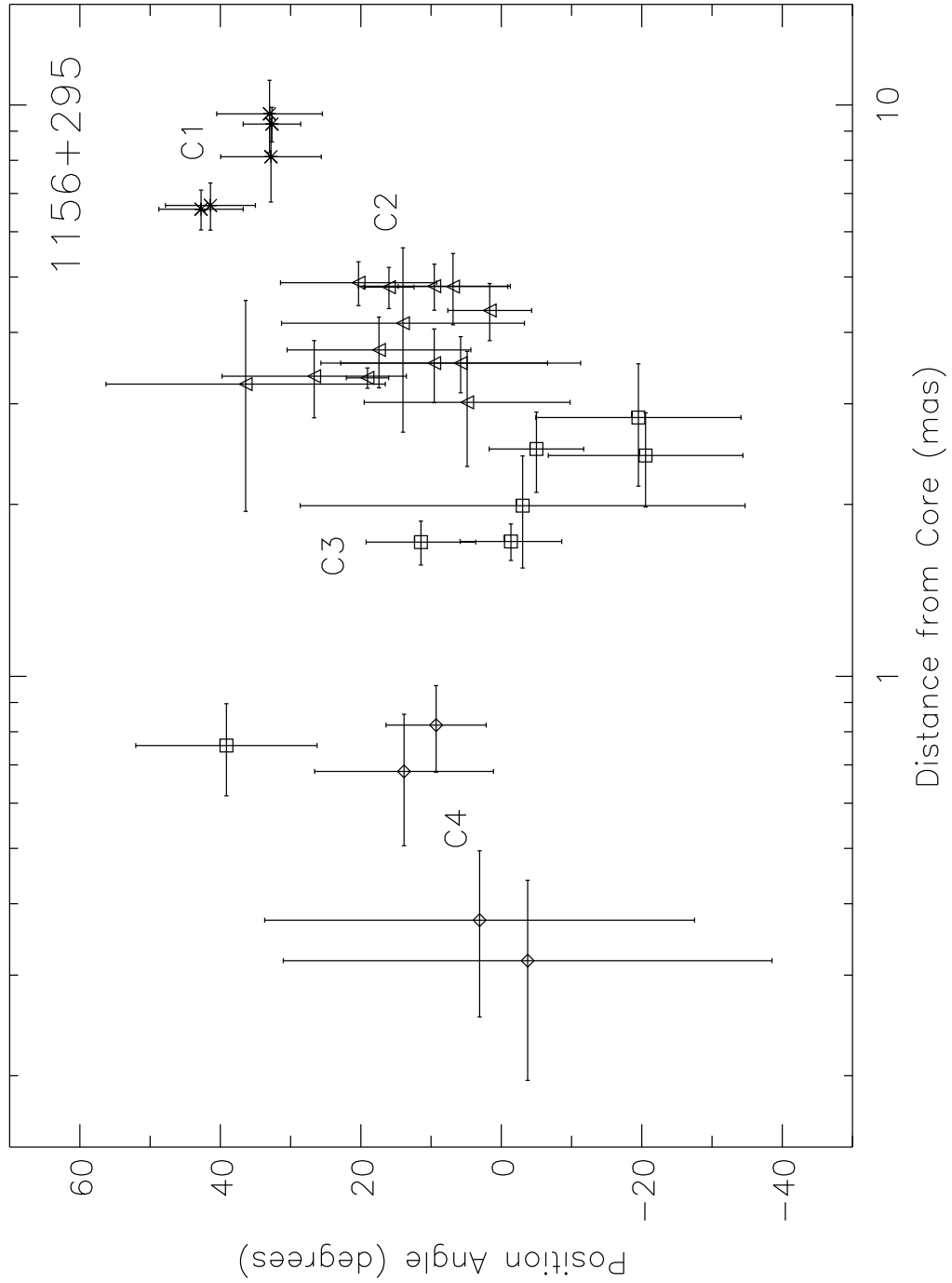


Figure 10: Measured positions of all components at all frequencies and all epochs for 1156+295. The x -axis shows the distance from the core on a logarithmic scale and the y -axis shows the position angle, measured from north through east. Asterisks show measured positions of C1, triangles C2, squares C3, and diamonds C4.

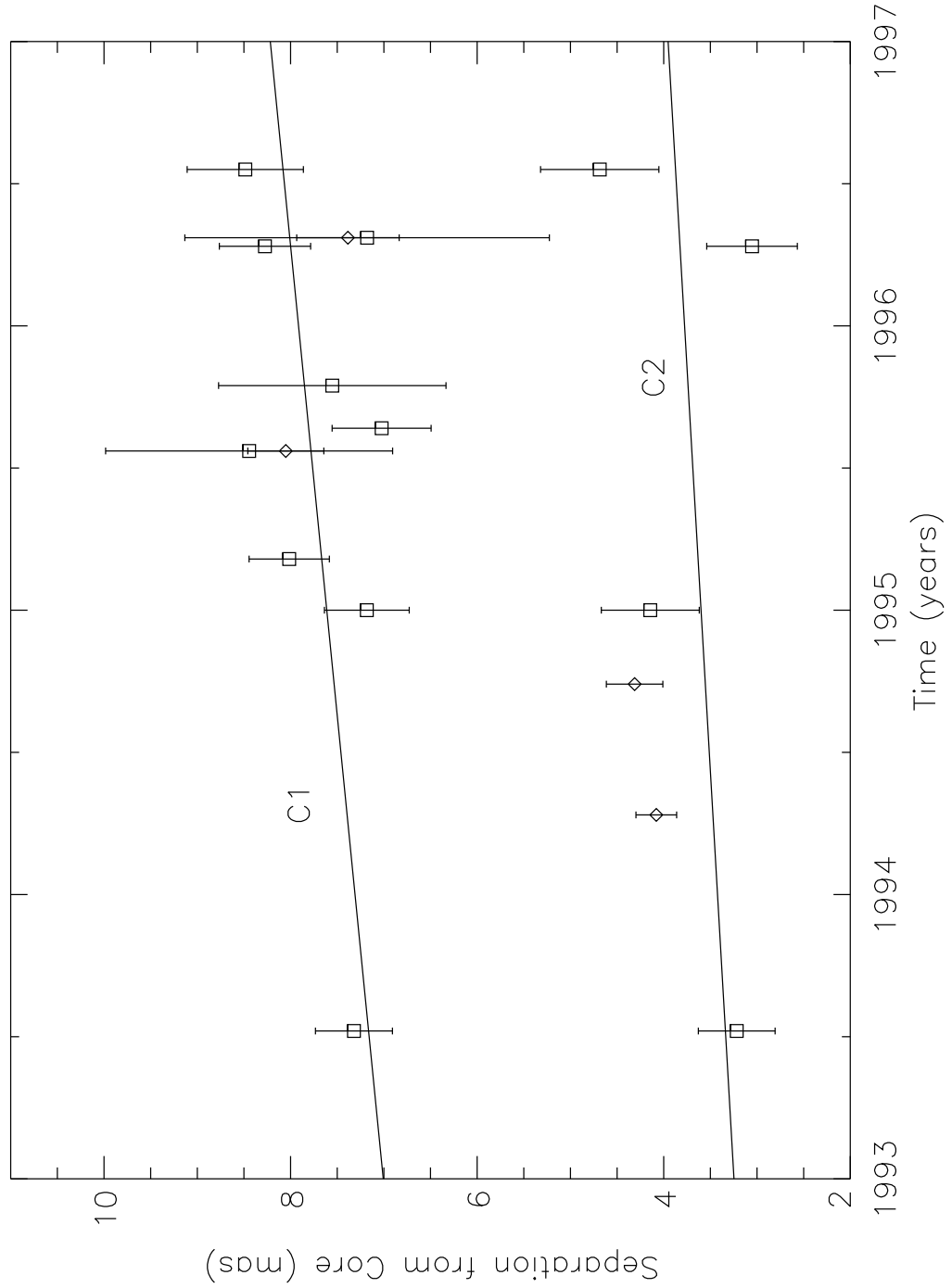


Figure 11a: Separation of components C1 and C2 in 1606+106. Squares represent the 2 GHz positions and diamonds the 8 GHz positions. The lines are the best fits to motion with constant velocity for the 2 GHz positions.

Figure 11*b* shows our measurements of the distances from the core of the inner components: C3, C4, and C5. These components are all too close to the core to be detected at 2 GHz. All of our observations of these components are at 8 GHz and are combined with some VLBA detections at 15 GHz. The measured velocities for components C3, C4, and C5 are 3.4 ± 1.7 , 2.4 ± 1.1 , and $0.0 \pm 0.9 h^{-1}c$ respectively. C3 and C4 move outward superluminally, while C5 is stationary with respect to the core. VC94 point out that the large number of stationary components found in core-dominated quasars precludes their being part of a continuous distribution of Lorentz factors, and they probably represent a different phenomenon from the more rapidly moving components. If we therefore exclude the velocity measurement of C5, the velocities of the other four components are consistent with all of these components moving at the same average velocity of $2.9 \pm 0.9 h^{-1}c$.

We have more measured component positions for this quasar than for any other; a total of 51 measured component positions are plotted in Figure 12. To aid comparison with the 8 GHz positions, the 2 GHz and 15 GHz radii have been adjusted by the observed magnitude of frequency-dependent separation in this source. Each component’s motion is well fit by a constant position angle. The motions of C1, C2, and C3 are all well fit by motion along the same position angle, $-38.2 \pm 1.0^\circ$, and the position angles of C4 and C5, $-55.3 \pm 2.3^\circ$ and $-77.5 \pm 4.8^\circ$ respectively, differ significantly from this and from each other. In this source each component could continue moving along the position angles given here, or C4 and C5 could move toward higher position angles to join the path defined by C1, C2, and C3. If these component positions do define a continuous path, then this path has only a gradual change in position angle which then becomes constant around 2 mas, in contrast to the hypothetical paths in CTA 26 and 1156+295, which had oscillations in position angle.

5. Discussion

5.1. 0202+149 as a Compact F Double

Analysis of the structure of VLBI images, along with large-scale source properties, has enabled VLBI sources to be classified into a number of morphological groups (e.g. Pearson & Readhead 1988, hereafter PR88). Most of the EGRET blazars imaged with VLBI show the core-dominated, flat-spectrum, core-jet morphology characteristic of strong beaming and can be classified into the *very compact*, *compact*, or *asymmetric I* categories in the PR88 scheme. All of the EGRET sources we have studied in detail have conformed to this expected morphology, with the exception of 0202+149. This source distinguishes itself in our VLBI images by having a simple double morphology at 2 GHz and by being the only source, out of the five for which we have measured apparent velocities, which exhibits no

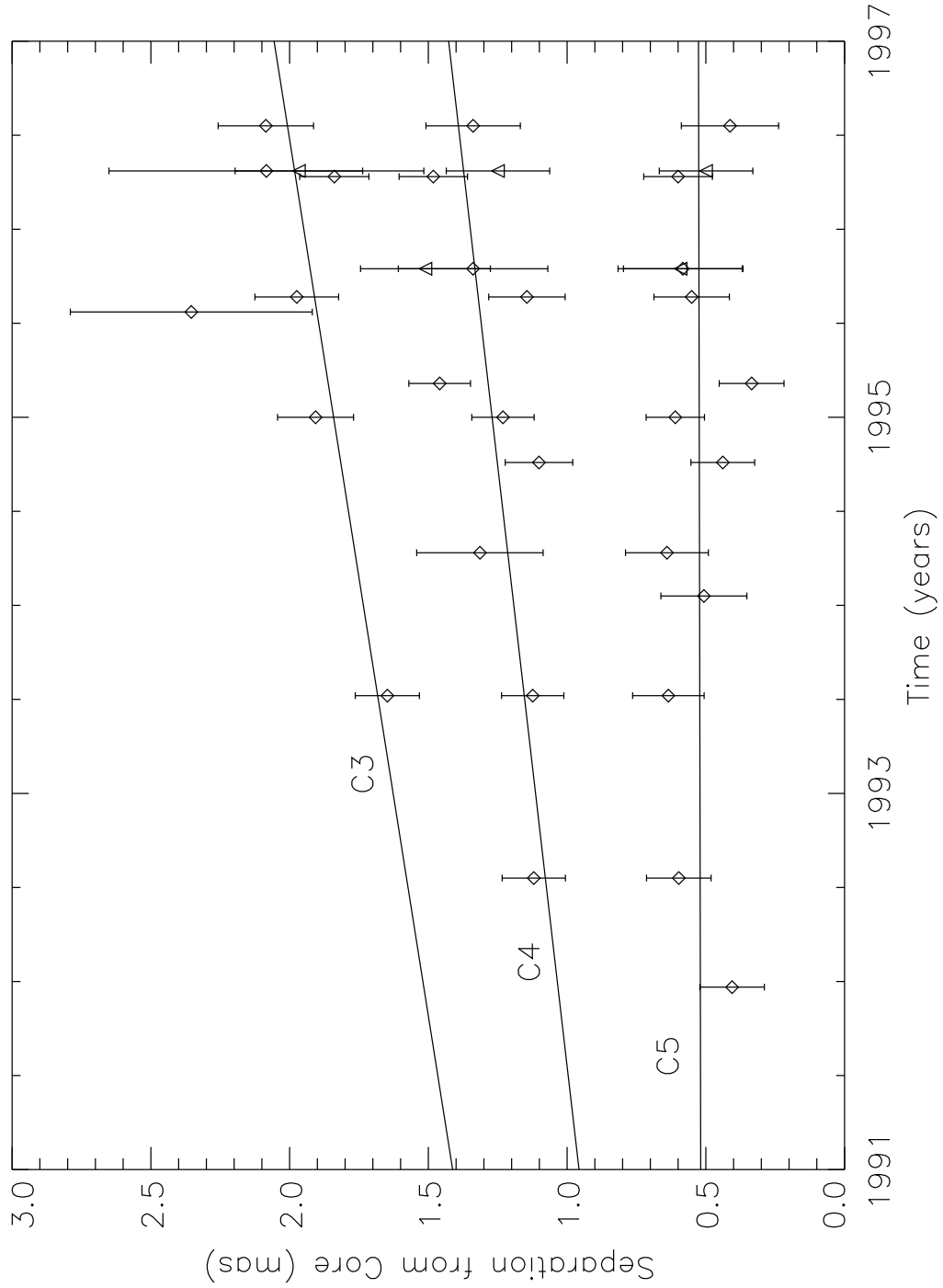


Figure 11b: Separation of components C3, C4, and C5 in 1606+106. Diamonds represent the 8 GHz positions and triangles the 15 GHz positions. The lines are the best fits to motion with constant velocity for the 8 GHz positions.

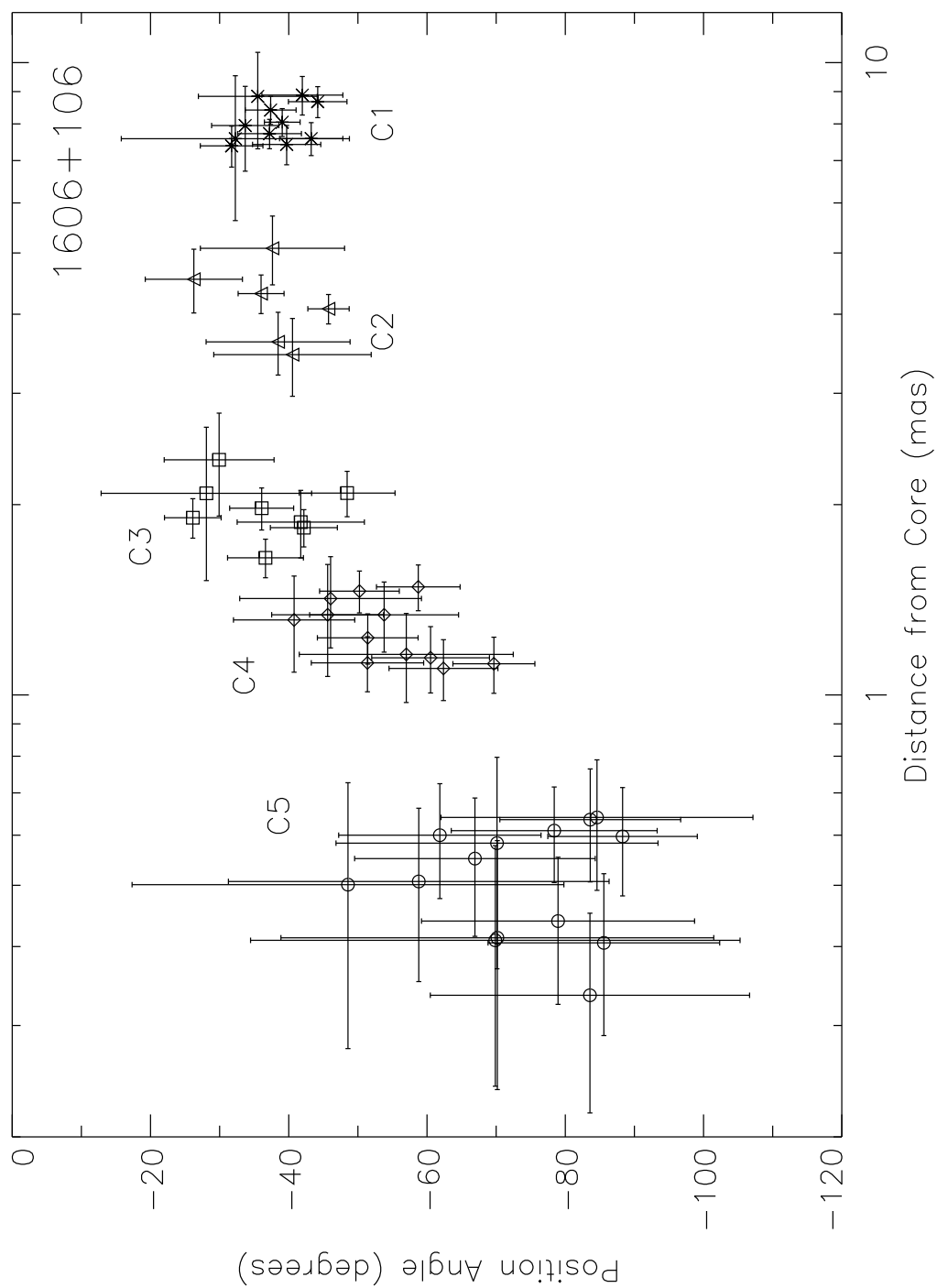


Figure 12: Measured positions of all components at all frequencies and all epochs for 1606+106. The x -axis shows the distance from the core on a logarithmic scale and the y -axis shows the position angle, measured from north through east. Asterisks show measured positions of C1, triangles C2, squares C3, diamonds C4, and circles C5.

apparent motion of the components. This source is unusual for an EGRET source in its large-scale properties as well. It is unresolved in VLA images (Murphy, Browne, & Perley 1993), has a low radio polarization of 0.2% (Perley 1982), and has a relatively small radio variability ($V=0.3$ from the UMRAO online database³, where $V=\Delta S/ < S >$). These properties all match the properties of the compact F double class, and we can identify 0202+149 as a new compact F double source. The compact double sources were first identified by Phillips and Mutel (1982), and this class of sources was divided according to their spectral index into compact S ($\alpha < -0.5$) and compact F ($\alpha > -0.5$) doubles by PR88.

Detailed studies of the compact double sources by Conway et al. (1994) have shown that the compact S and compact F doubles are likely to be very different physical phenomena and that the compact F doubles are probably physically more similar to the core-jet sources than to their steep-spectrum counterparts. They suggest that the components of compact S doubles are the termination points of oppositely directed jets, while compact F doubles are an unusual form of core-jet source with a bright, stationary jet component. The EGRET detection of 0202+149 strengthens the conclusion of Conway et al. (1994) that the compact F double sources are just an unusual form of core-jet source and are physically very different from the “terminating jet” interpretation of compact S doubles, where we would not expect to see γ -ray emission.

Observations of γ -rays from 0202+149 imply that the source is strongly beamed. This strong beaming, together with the very low apparent velocities, means that the jet must be aligned extremely close to the line-of-sight if the component velocities reflect the bulk motion of material in the jet. Indications of strong beaming have been seen in the other compact F doubles in the form of high jet/counterjet brightness ratios. Conway et al. (1994) show that the stationary components then imply such a small angle of the jet to the line-of-sight that the probability of observing these sources is very low. They suggest two models to explain the stationary components of compact F doubles, although the large-scale properties of these sources, which also make them quite different from normal core-jet sources, remain to be explained. The components could represent standing shocks in the jet, implying that the component velocities are much less than the bulk velocity of jet material. Alternatively, the components could be due to relativistic flow close to the line-of-sight along a curving jet, and since a curving jet samples a range of angles to the line-of-sight, the arguments suggesting a low probability of detection would not apply. Since both of these models allow for bulk relativistic motion close to the line-of-sight, the

³<http://www.astro.lsa.umich.edu/obs/radiotel/umrao.html>

detection of γ -rays from a compact F double seems compatible with either model.

5.2. Correlations between Flares and Component Ejections

It is interesting to see if VLBI component ejections correlate with outbursts in the light curves of these sources. Correlations between the emergence of new VLBI components and radio flares have been noted by many authors, e.g, Mutel et al. (1994, 1990), Zensus et al. (1990). Such a correlation is not surprising; since newly emerged VLBI components typically have a high radio flux, it is not unexpected that they would contribute significantly to the total light curve. A more meaningful correlation would be if component ejections correlated with flares in the optical or γ -ray regimes. Then we would actually be observing the effects of enhanced activity in the central engine as they propagated down the jet. In the common shock interpretation of VLBI components, γ -ray and optical emission could originate in these compact energetic shocks as they form and move out from the core. After some time, typically zero to several hundred days (Tornikoski et al. 1994), the component becomes optically thin to lower frequency radio emission, causing the observed brightening in the radio. Also at about this time, depending on source distance and VLBI resolution, the component becomes resolved from the “core” in VLBI observations, where the VLBI “core” is simply the point at which the jet becomes optically thick. Such a detailed scenario in which the γ -ray emission is due to a propagating discontinuity (corresponding to a jet component observed with VLBI) in a Poynting flux jet, and where the delay of the radio emission is due to self-absorption or free-free absorption by external plasma, has been proposed by Romanova & Lovelace (1996). Reich et al. (1993) have observed enhanced radio emission with a delay of several months relative to the EGRET detection in some sources. Conversely, some models predict that there should be no correlation between VLBI component ejections and γ -ray flares. In the model of Punsly (1996), the VLBI jet and the γ -ray jet are two separate jets, so we would not expect any correlation between them.

Correlations between optical flares and the formation of VLBI components have been noted — for example, component C9 of 3C273 (Krichbaum et al. 1990) and components K1 and K3 of OJ287 (Vicente et al. 1996) — although these references also mention that there are optical flares with no subsequent VLBI components and VLBI components which have no associated optical flares. Gabuzda & Sitko (1994) see variations in optical polarization accompanying component ejections in OJ287 and 3C279. The lack of detection of a VLBI component following a flare could be due to extremely short-lived components. Abraham et al. (1994) have detected components with lifetimes as short as one year in 3C273, and they suggest the ejection rate of these components may be much higher than previously

thought. High frequency VLBI observations by Krichbaum et al. (1995) have revealed newly emerged components which appear correlated with preceding EGRET flares in 0528+134, 0836+710, and 3C454.3. Similar results have been obtained for 3C279 (Wehrle et al. 1996). These results indicate that γ -ray flares may be related to the production of observed jet components.

We have calculated the epoch of zero separation for each moving component in all of our sources. These times are listed in Table 5. We list only those components that have emerged recently enough that correlated flux observations might exist, i.e., the outer components of all sources and the slow-moving and stationary components of 0202+149 and 1606+106 are not listed. The 1σ errors in the velocities were used to calculate the errors in the separation times; note that this does not produce symmetric errors. The recent ejections of C2 and C3 in CTA 26, and C3 and C4 in 1156+295, appear to correlate with outbursts in the historic radio and optical light curves. These outbursts are listed in Table 5. For CTA 26 the ejection times of C2 and C3 correlate with the two largest radio flares since 1990 (M. Aller 1996, private communication). Smith et al. (1993) also show CTA 26 entering a more active optical state around 1990. For 1156+295, the ejection of C3 seems to correlate with a very large optical flare in 1985, and the later ejection of C4 corresponds to a peak in the high-frequency radio light curve (Tornikoski et al. 1994).

Table 5: Component Ejection Times

Source	Comp.	Ejection Time	1σ Time Range	Possible Correlated Outbursts
CTA 26	C2	1991 Jun	1990 Nov - 1991 Nov	1990; 4.8, 8, and 14.5 GHz
	C3	1993 Apr	1993 Jan - 1993 Jul	1993; 4.8, 8, and 14.5 GHz
1156+295	C3	1985 Sep	1984 Jul - 1986 Jul	early 1985; optical mid 1985; 90 GHz
	C4	1991 Mar	1989 Jun - 1992 Jan	1990; 37 and 90 GHz

We are particularly interested in possible correlations with EGRET flares. We found in Paper I that the separation time of C5 in 1611+343 was during a high state of γ -ray activity. For the sources studied in detail in this paper, a γ -ray flare can be identified in the EGRET light curves of CTA 26, 1156+295, and 1606+106. Figure 13 shows the EGRET light curves for these three sources along with that for 1611+343, which is shown for completeness. These light curves have been constructed from the data in Mukherjee et al. (1997). All of these sources have a γ -ray variability index greater than 1 (Mukherjee et al. 1997), indicating strong variability. These plots also show the time ranges for the ejections of VLBI components which have emerged during the lifetime of EGRET. The

only component whose ejection time correlates with an observed high level of γ -ray activity is component C5 of 1611+343. EGRET upper limits recorded during the ejection times of the other components do not necessarily mean there was no correlated flare, because such a flare could have occurred when EGRET was not observing the source. Actual evidence of no correlation must instead come from EGRET flares with no accompanying VLBI components. As yet, no components have been detected emerging as a result of the flares of CTA 26, 1156+295, and 1606+106. Lower limits can be set on the time at which such a component could have emerged by assuming it travels at the average speed of components in that source and would be resolved by the time it reached 0.4 mas from the core (the distance of C2 in 0202+149 and C5 in 1606+106). These lower limits are shown as right-facing arrows on the light curves of CTA 26, 1156+295, and 1606+106. For CTA 26 and 1606+106 these times are only slightly later than the observed γ -ray flare, so a somewhat slower than average component may yet be seen (in fact, such a component has been reported recently in high-frequency VLBA observations of CTA 26 by Hallum et al. (1997)), but for 1156+295 it appears there is definitely no component correlated with the 1993 EGRET flare. If there was a correlated component in this source, then it is likely that it was so short lived that it was not detected. These data give no indication that EGRET flares are correlated with VLBI component ejections, contrary to the correlations observed by other authors discussed earlier in this section. However, since the observations by other authors were at higher frequency and resolution — and thus better able to detect short-lived components — such a correlation may still be possible.

5.3. Calculation of Doppler Beaming Factors

Since the value of the apparent superluminal velocity is a function of both the Lorentz factor Γ and the angle to the line-of-sight θ , knowledge of the apparent speeds alone is sufficient only to place a lower limit on Γ or an upper limit on θ . Another parameter of the flow which depends on both Γ and θ is the ratio of observed to emitted frequency, or Doppler factor, $\delta = [\Gamma(1 - \beta \cos \theta)]^{-1}$. If both δ and the apparent velocity are known, the Lorentz factor and angle to the line-of-sight of the flow can in principle be determined. This assumes that the Lorentz factor of the pattern speed seen in the superluminal motions, Γ_p , is the same as the Lorentz factor of the bulk fluid flow causing the Doppler boosting, Γ_b , which for some sources may be an incorrect assumption.

There have been several methods used to determine values of δ for AGNs. One method, (see e.g. Marscher 1987; Ghisellini et al. 1993, hereafter GPCM), assumes that the X-ray flux from the source is produced by the synchrotron self-Compton (SSC) process. The

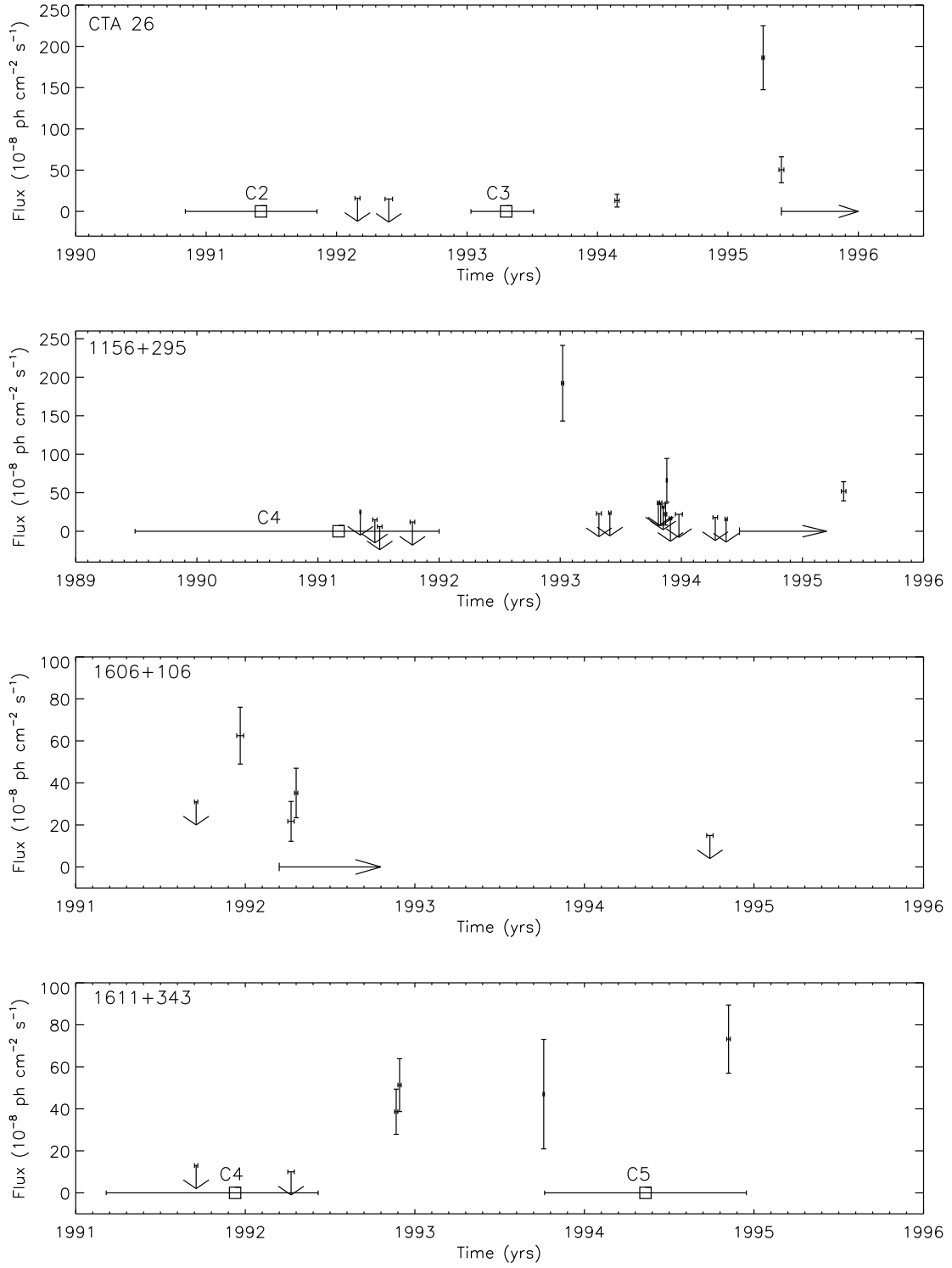


Figure 13: EGRET light curves with component ejection times.

expected SSC emission from a VLBI component depends on δ and on parameters which can be estimated from the VLBI images. A lower limit to the Doppler factor, δ_{SSC} , is obtained because for values of δ_{SSC} which are too low, the calculated X-ray flux from a component is greater than the actual X-ray flux from the source. Another method of calculating δ (e.g., Dondi & Ghisellini 1995, hereafter DG95) can be applied to γ -ray sources by demanding that the optical depth due to pair-production be low enough for γ -rays to escape. This optical depth depends on δ , so a lower limit, δ_γ , can be obtained by setting the optical depth equal to 1. Readhead (1994) notes that intrinsic brightness temperatures of sources do not vary much from the “equipartition brightness temperature” — the brightness temperature at which there is equipartition of energy between the radiating particles and the magnetic field. The observed brightness temperature can be compared with the equipartition brightness temperature to determine the equipartition Doppler factor, δ_{eq} (Güijosa & Daly 1996, hereafter GD96). Each of these methods has drawbacks; the first two give only lower limits to δ and the third assumes equipartition, which may not be valid in all sources. A lower limit on the Doppler factor implies that when these Doppler factors are compared with apparent superluminal velocities, only lower limits to Γ and upper limits to θ can be obtained, although these limits are often better than those obtained using the apparent velocity alone.

We have calculated δ_{SSC} for the core components of the sources in our sample. Unfortunately, these Doppler factors depend on powers as high as the square of sometimes poorly known quantities such as the angular size of the component and the frequency and flux at the peak of the synchrotron spectrum. Since we only have observations at two frequencies, we are not able to precisely determine the peak of the synchrotron spectrum, and in general we assume a turnover at 8 GHz if the spectrum is rising over the observed range, a turnover at 2 GHz if it is falling, or a turnover at 5 GHz if it is flat. We have high resolution for each of our observing frequencies, which should give relatively accurate measurements of the core angular size. We also average the Doppler factors calculated at the individual epochs to obtain the estimate of δ for each source. This averaging should alleviate some of the error introduced by inaccurate measurements of angular size or flux density. Although GPCM, DG95, or GD96 have calculated Doppler factors for all of our sources except 0202+149, they all used single-epoch single-frequency VLBI data, and hence were forced to assume that the frequency of observation was the turnover frequency. We hope our multi-epoch dual-frequency data may provide better estimates of these Doppler factors.

We use equation (1) of GPCM to calculate δ_{SSC} . This equation is

$$\delta_{SSC} = f(\alpha) S_m \left[\frac{\ln(\nu_b/\nu_m) \nu_x^\alpha}{S_x \theta_d^{6-4\alpha} \nu_m^{5-3\alpha}} \right]^{1/(4-2\alpha)} (1+z),$$

where $f(\alpha) \approx -0.08\alpha + 0.14$, S_m is the flux density (in Jy) at the turnover frequency ν_m (in GHz), S_x is the X-ray flux density (in Jy) at frequency ν_x (in keV), ν_b is the synchrotron high-frequency cutoff (assumed to be 10^{14} Hz, (GPCM)), θ_d is the angular diameter of the radio core at the turnover frequency (in mas), and the sign of α has been changed to reflect the convention used in this paper. This equation assumes the radiating component is a homogeneous sphere. While more sophisticated geometries such as conical jets have been used by some authors, e.g. Unwin et al. (1994), they also require more sophisticated multi-frequency VLBI data in order to constrain them. In keeping with GPCM, we use an optically thin spectral index of $\alpha = -0.75$ and use X-ray fluxes from DG95. GD96 report two correction factors that must be applied to this equation: a factor of 1.8 in the angular size and a factor of 2 in the flux at the spectral peak. When we calculated Doppler factors for 1611+343 in Paper I, we were aware of only the first of these correction factors, so we give fully corrected values for 1611+343 here. Values of the Doppler factors and the corresponding limits to Γ and θ are given in Table 6. Note that since $\Gamma(\delta)$ has a minimum of $\Gamma^* = (\beta_{app}^2 + 1)^{1/2}$, where β_{app} is the apparent velocity, at $\delta = \Gamma^*$, then if $\delta < \Gamma^*$ the lower limit obtained on Γ is the same as that obtained from the apparent velocity alone.

The values of δ_{SSC} found for CTA 26 and 1156+295 agree well with the values found for these sources by GPCM and GD96. The values of δ_{SSC} found for 1606+106 and

Table 6: Doppler Beaming Factors

Source	δ_{SSC}	β_{app} ^a	Γ ^b	θ ^c (deg)
0202+149	18.0	0.4	9.0	0.15
CTA 26	12.8	8.9	9.5	4.2
1156+295	4.4	5.2	5.3	12.9
1606+106	15.3	2.9	7.9	1.4
1611+343	16.6	11.4	12.2	3.2

^aApparent velocity. Values are the weighted average of the apparent velocities of all components except for 1606+106, where the stationary component C5 is excluded, and 1611+343, where the velocity of the inner component is used since the components have different velocities.

^bLower limit on the Lorentz factor calculated from δ_{SSC} and β_{app} .

^cUpper limit on the angle of the jet to the line-of-sight calculated from δ_{SSC} and β_{app} .

1611+343 are considerably higher than the corresponding values found by DG95, possibly due to higher resolution of our VLBI observations. The values of δ_{SSC} calculated for these five sources are considerably higher than the values of δ_γ calculated for these same sources by DG95. In fact, the average value of δ_{SSC} for the entire DG95 sample is higher than the average value of δ_γ for the same sample, which implies that the γ -ray optical depth in these sources is considerably less than 1, since a value of unity is assumed in the calculation of δ_γ .

The angles to the line-of-sight listed in Table 6 are all relatively small, as is expected for strongly beamed sources. In particular, the high Doppler factor and low apparent velocity of 0202+149 imply a very small angle to the line-of-sight of 0.15° . The chance probability of a source having such a small angle to the line-of-sight is only 3.4×10^{-6} . Such an unreasonably small angle must imply that the pattern speed Γ_p is much less than the bulk fluid speed Γ_b (this equality being assumed in the calculation of Γ and θ), or that the stationary components represent points along a curving jet where the jet is directly aligned with the line-of-sight. One of these situations is what we would expect, given the nature of 0202+149 as a compact F double (see § 5.1). A similar situation may exist for 1606+106, since it also has a low β_{app} but high δ . The other sources also have angles close to the line-of-sight, and in fact all except 1156+295 are on the small angle side of the maximum in the $\beta_{app}(\theta)$ relation, where the apparent velocity *decreases* with decreasing angle to the line-of-sight. If we consider a Hubble constant of 50 rather than 100, thus doubling the values of β_{app} , the angles to the line-of-sight become larger for all sources except 1156+295, and the angular solutions for CTA 26 and 1611+343 move to the large angle side of the maximum in the $\beta_{app}(\theta)$ relation.

5.4. Comparison of EGRET and non-EGRET Sources

One of the major questions to be answered about the EGRET sources is why some of the sources sharing the common characteristics of EGRET blazars are not detected in γ -rays. Some possible reasons for this mentioned by von Montigny et al. (1995b) are that there may be intrinsic differences between the detected and undetected sources; that all blazars emit γ -rays but some are not currently seen due to long timescale variability; and that the γ -ray emission may be beamed more narrowly than the radio emission. VLBI observations are uniquely suited to testing this third possibility. Many of the source properties observed with VLBI, including the apparent superluminal velocity, β_{app} , depend on the angle of the jet to the line-of-sight, so in principle the jet orientation angles of the EGRET and non-EGRET sources can be compared. Note that the EGRET and non-EGRET sources do not necessarily have a bimodal distribution in their ratio of γ -ray

flux to radio flux, as the radio-loud and radio-quiet quasars do in their ratio of radio to optical flux (e.g. Rawlings 1994). However, since Mattox et al. (1997) show that there is a correlation between average 5 GHz radio flux and peak γ -ray flux, and many of the strongest radio blazars have not been detected by EGRET, there is at least a very large scatter in the ratio of γ -ray flux to radio flux that remains to be explained.

We decided to compare the average values of β_{app} for the EGRET and non-EGRET sources to see if there is a significant difference between the two groups. We use the speeds of all VLBI components measured in this work, Paper I, and Paper II, along with the collected apparent velocity data of VC94 and some more recent VLBI observations of the EGRET sources 0420-014 (Wagner et al. 1995), 0528+134 (Krichbaum et al. 1995; Pohl et al. 1995), and 1633+382 (Barthel et al. 1995). Recent observations of 1730-130 (Bower et al. 1997) are not included since the superluminal motion is only inferred from the timing of flux outbursts. A similar comparison has been done by Tingay et al. (1996); however, we include the speeds of 15 new VLBI components measured in this paper, Paper I, and Paper II — thus approximately doubling the available sample for EGRET sources — and we also use the data of VC94 somewhat differently. For the EGRET sources, we exclude the BL Lacs, and we consider only the core-dominated quasars from VC94, because Gabuzda et al. (1994) show that the β_{app} values of BL Lacs and quasars are quite different. We also combine the apparent velocity data using weighted averaging, so we exclude any apparent velocity measurement published without an associated error. When multiple components have been measured in a single source, we take the weighted average of the component speeds to form an average value for that source; this is exactly equivalent to forming the weighted average of *all* components from *all* sources. Since VC94 remark that the large number of stationary components found in core-dominated quasars implies that they probably represent a different phenomenon from the more rapidly moving components, we also exclude components where the velocity measurement and associated error are consistent with no motion. We find that the two groups of EGRET and non-EGRET sources have the same average apparent velocity of $5.5h^{-1}c$, with the standard deviations of the distributions being 2.7 and $2.4 h^{-1}c$ respectively. Histograms of these apparent velocities are shown in Piner (1998). We find no evidence that the EGRET and non-EGRET sources have different apparent velocities, in agreement with Tingay et al. (1996).

Apparent velocity is probably not the best indicator of orientation. The graph of β_{app} vs. θ has a maximum at $\sin\theta = 1/\Gamma$, and below this maximum the apparent velocity decreases as the source moves closer to the line-of-sight. If a significant number of EGRET sources are located on the small angle side of this maximum, they could actually have a lower average apparent velocity than other sources while still being closer to the line-of-sight. A better indicator of orientation is a function which increases monotonically

as the angle to the line-of-sight decreases, such as the Doppler factor δ or the ratio of core to extended flux, or core dominance parameter, R .

We have investigated the average values of δ and R for EGRET and non-EGRET sources using the values of δ_{SSC} from GPCM, DG95, GD96, Guerra & Daly (1997), and this paper; values of R from GPCM, DG95, and Murphy et al. (1993); and using the set of EGRET sources from Mukherjee et al. (1997). The average values for δ_{SSC} and R of the EGRET and non-EGRET sources are given in Table 7, where we have used the same source classifications used by GPCM. The average values of δ_{SSC} for the EGRET and non-EGRET sources are the same within the errors, which may simply reflect the large uncertainties in determining δ_{SSC} . The only significant difference in the R values occurs for the LPQs, where the EGRET LPQs have an R value significantly higher than the non-EGRET LPQs. This implies that the EGRET LPQs are more strongly beamed than the non-EGRET LPQs and, if degree of polarization increases with decreasing angle to the line-of-sight, implies that the EGRET LPQs have an angle to the line-of-sight typical of HPQs. Since degree of polarization is variable, this suggests that the EGRET LPQs may really be HPQs which were classified during a low-polarization state.

Table 7: Average Values of δ_{SSC} and $\log R$

Source Type	EGRET sources		non-EGRET sources	
	δ_{SSC}^b	$\log R$	δ_{SSC}	$\log R$
BL Lacs	4.0 ± 1.5	1.76 ± 0.38	3.1 ± 0.7	1.63 ± 0.21
CDQs ^a	7.9 ± 1.4	1.27 ± 0.15	7.3 ± 1.0	1.08 ± 0.10
HPQs	8.5 ± 1.9	1.21 ± 0.19	9.0 ± 1.3	1.33 ± 0.21
LPQs	7.1 ± 2.1	1.43 ± 0.25	6.8 ± 1.7	0.93 ± 0.10

^aCore Dominated Quasars. Combination of the HPQs and LPQs.

^bErrors given are the standard deviation of the mean.

We also compared the misalignment angle distribution of the EGRET blazars to that of the non-EGRET blazars, where the misalignment angle is the difference between the VLBI and VLA-scale position angles. For the EGRET sources we measured misalignment angles using the method of Xu et al. (1994) for all sources where images were available in the literature, as well as using the new images from this paper, Paper I, and Paper II. A complete listing of these misalignment angles is given by Piner (1998). We compared this misalignment angle distribution to that for HPQs in general using the results from the combined Pearson & Readhead and first Caltech-Jodrell Bank surveys presented by Xu et

al. (1994) and found that EGRET sources do not preferentially belong to either the aligned or the misaligned population, but follow the distribution typical of highly polarized sources in general. These results independently confirm similar results found recently by Bower et al. (1997).

In conclusion, we do not find strong evidence that we are viewing γ -ray sources any closer to the line-of-sight than is typical for an HPQ source. Moellenbrock et al. (1996), in a survey of core-dominated radio sources, found that the γ -ray sources occupy the high end of their brightness temperature distribution, indicating that the γ -ray sources are among the most highly beamed in their sample. However, their sample includes both high and low polarization core-dominated quasars. Unified schemes (Guerra & Daly (1997), Teräsanta & Valtaoja (1994)) indicate that LPQs typically have a larger angle to the line-of-sight than HPQs. If the KS test done by Moellenbrock et al. (1996) is redone using only the HPQ sources from their sample and the latest list of EGRET sources, the significance of the difference between the brightness temperature distributions of the EGRET and non-EGRET sources drops below 95%. We conclude that VLBI observations are consistent with the average opening angle for the γ -ray emission being approximately equal to the average viewing angle for an HPQ. If this is so, then the reason some HPQs are not seen in γ -rays is probably due to intrinsic source differences or time variability. Nair (1997) has stated that cluster analysis shows that γ -ray sources have larger amplitudes of optical variability and are bluer at larger redshifts. Punsly (1996) has found that γ -ray quasars have larger mm spectral peaks relative to their cm spectral peaks than other core-dominated quasars. Both of these may be evidence that there are some intrinsic differences between the EGRET and non-EGRET sources.

6. Conclusions

We have presented VLBI images of the EGRET quasars 0202+149, CTA 26, and 1606+106. We have detected superluminal motion in two of these sources, CTA 26 and 1606+106; such superluminal motion is expected from highly beamed γ -ray blazars. The high Doppler factor derived for 0202+149 also indicates that it is strongly beamed, the stationary jet components in this source can be interpreted as standing shocks or flow very close to the line-of-sight. The quasar 0202+149 satisfies all the criteria of the compact F double morphology class as given by PR88. We have also investigated the shapes of the VLBI jets in all of these sources, as well as in 1156+295, and have found they all possess apparently bent jets. We have detected non-radial motions of components in CTA 26 and 1156+295. It has been noted by some authors (Krichbaum et al. 1995; Wehrle et al. 1996),

and is expected from some theoretical models, that VLBI components appear subsequent to γ -ray flares. We have not yet detected any components emerging subsequent to the γ -ray flares in CTA 26, 1156+295, and 1606+106, although the only source which has a lower limit on the ejection time of such a component that is significantly later than the γ -ray flare in that source is 1156+295.

The observations of the three sources presented here, along with the observations of 1611+343 and 1156+295 presented in Papers I and II, significantly increase the number of EGRET sources for which detailed VLBI monitoring data are available. Such an increase makes comparisons between properties of the EGRET and non-EGRET populations more significant. We have compared the misalignment angle distribution of EGRET sources to the distribution for blazars as a whole and find that the EGRET sources do not preferentially belong to the aligned or the misaligned population. We have also compared the average values of the apparent velocity, the Doppler factor, and the core dominance parameter for the EGRET sources with the same quantities for the non-EGRET sources. We find no significant difference in these quantities between the two groups. We thus find no indication that the EGRET blazars are more strongly beamed than the non-EGRET blazars, although the estimated errors and the scatter of individual sources are rather large, particularly for estimates of the Doppler factor. This paper, along with Paper I and Paper II, shows the great usefulness of archived geodetic VLBI data in producing high quality, densely time sampled series of VLBI images for use in astrophysical studies. The Washington VLBI correlator's geodetic database continues to be a potential source for such studies.

We acknowledge the support of the VLBI staff at the Naval Observatory and the EGRET team at NASA/GSFC. We also acknowledge helpful discussions and communication of data in advance of publication from Margo Aller, Steve Bloom, Alan Fey, and Bob Hartman. Additionally, we acknowledge the referee for his/her helpful comments and suggestions, particularly in pointing out the dangers of mentally equating EGRET and non-EGRET blazars to radio-loud and radio-quiet quasars. This research has made use of the United States Naval Observatory (USNO) Radio Reference Frame Image Database (RRFID), data from the University of Michigan Radio Astronomy Observatory which is supported by the National Science Foundation and by funds from the University of Michigan, and the NASA/IPAC extragalactic database (NED) which is operated by the Jet Propulsion Laboratory, Caltech, under contract with the National Aeronautics and Space Administration.

REFERENCES

- Abraham, Z., Carrara, E.A., Zensus, J.A., & Unwin, S.C. 1994 in NRAO Workshop 23, Compact Extragalactic Radio Sources, ed. J.A. Zensus & K.I. Kellermann (Green Bank:NRAO), 87
- Alberdi, A., Marcaide, J.M., Marscher, A.P., Zhang, Y.F., Elósegui, P., Gómez, J.L., & Shaffer, D.B. 1993, *ApJ*, 402, 160
- Barthel, P.D., Conway, J.E., Myers, S.T., Pearson, T.J., & Readhead, A.C.S. 1995, *ApJ*, 444, L21
- Begelman, M.C., Blandford, R.D., & Rees, M.J. 1980, *Nature*, 287, 307
- Biretta, J.A., Moore, R.L., & Cohen, M.H. 1986, *ApJ*, 308, 93
- Bondi, M. et al. 1996, *A&A*, 308 415
- Bower, G.C., Backer, D.C., Wright, M., Forster, J.R., Aller, H.D., & Aller, M.F. 1997, *ApJ*, 484, 118
- Britzen, S., Krichbaum, T.P., Steffen, W., Witzel, A., & Schalinski, C.J. 1994 in NRAO Workshop 23, Compact Extragalactic Radio Sources, ed. J.A. Zensus & K.I. Kellermann (Green Bank:NRAO), 251
- Charlot, P. 1990, *A&A*, 229, 51
- Charlot, P. 1993, in *Sub-arcsecond Radio Astronomy*, ed. R.J. Davis & R.S. Booth (Cambridge:Cambridge Univ. Press), 218
- Condon, J.J. 1997, *PASP*, 109, 166
- Conway, J.E., Myers, S.T., Pearson, T.J., Readhead, A.C.S., Unwin, S.C., & Xu, W. 1994, *ApJ*, 425, 568
- Dondi, L. & Ghisellini, G. 1995, *MNRAS*, 273, 583
- Fey, A.L., & Charlot, P. 1997, *ApJS*, 111, 95
- Fey, A.L., Clegg, A.W., & Fomalont E.B. 1996, *ApJS*, 105, 299
- Fey, A.L., Eubanks, T.M., & Kingham, K.A. 1997, *AJ*, 114, 2284
- Gabuzda, D.C., Mullan, C.M., Cawthorne, T.V., Wardle, J.F.C., & Roberts, D.H. 1994, *ApJ*, 435, 140
- Gabuzda, D.C., & Sitko, M.L. 1994, *AJ*, 107, 884
- Ghisellini, G., Padovani, P., Celotti, A., & Maraschi, L. 1993, *ApJ*, 407, 65
- Guerra, E.J. & Daly, R.A. 1997, *ApJ*, 491, 483

- Güijosa, A. & Daly, R.A. 1996, ApJ, 461, 600
- Hallum, J.C., Mattox, J.R., Marscher, A.P., Waltman, E., Teräsranta, H., Aller, H.D., & Aller, M.F. 1997, BAAS, 29, 1374
- Hardee, P.E. 1987, ApJ, 318, 78
- Hewitt, A. & Burbidge, G. 1989, ApJS, 69, 1
- Johnston, K.J. et al. 1995, AJ, 110, 880
- Kaastra, J.S. & Roos, N. 1992, A&A, 254, 96
- Krichbaum, T.P. et al. 1990, A&A, 237, 3
- Krichbaum, T.P., Britzen, S., Standke, K.J., Witzel, A., Schalinski, C.J., & Zensus, J.A. 1995, Proc. Natl. Acad. Sci., 92, 11377
- Linfield, R.P. et al. 1989, ApJ, 336, 1105
- Marscher, A.P. 1987, in Superluminal Radio Sources, ed. J.A. Zensus & T.J. Pearson (Cambridge:Cambridge Univ. Press), 280
- Mattox, J.R., et al. 1993, ApJ, 410, 609
- Mattox, J.R., Schachter, J., Molnar, L., Hartman, R.C., & Patnaik, A.R. 1997, ApJ, 481, 95
- Mukherjee, R. et al. 1997, ApJ, 490, 116
- McHardy, I.M., Marscher, A.P., Gear, W.K., Muxlow, T., Lehto, H.J., & Abraham, R.G. 1990, MNRAS, 246, 305
- McHardy, I.M., Marscher, A.P., Gear, W.K., Muxlow, T., Lehto, H.J., & Abraham, R.G. 1993, MNRAS, 261, 464
- Moellenbrock, G.A. et al. 1996, AJ, 111, 2174
- Murphy, D.W., Browne, I.W.A., & Perley, R.A. 1993, MNRAS, 264, 298
- Mutel, R.L., Denn, G.R., & Dryer, M.J. 1994 in NRAO Workshop 23, Compact Extragalactic Radio Sources, ed. J.A. Zensus & K.I. Kellermann (Green Bank:NRAO), 191
- Mutel, R.L., Phillips, R.B., Su, B., & Bucciferro, R.R. 1990, ApJ, 352, 81
- Nair, A.D. 1997, MNRAS, 287, 641
- Padrielli, L., et al. 1986, A&A, 165, 53
- Pearson, T.J. & Readhead, A.C.S. 1988, ApJ, 328, 114
- Perley, R.A. 1982, AJ, 87, 859
- Phillips, R.B. & Mutel, R.L. 1982, A&A, 106, 21

- Piner, B.G. 1998, PhD thesis, Univ. Maryland
- Piner, B.G. & Kingham, K.A. 1997a, ApJ, 479, 684
- Piner, B.G. & Kingham, K.A. 1997b, ApJ, 485, L61
- Pohl, M., et al. 1995, A&A, 303, 383
- Punsly, B. 1996, ApJ, 473, 152
- Rawlings, S. 1995, in *The First Stromlo Symposium: The Physics of Active Galaxies*, ed. G.V. Bicknell, M.A. Dopita, & P.J. Quinn (San Francisco:ASP), 253
- Readhead, A.C.S. 1994, ApJ, 426, 51
- Reich, W., Steppe, H., Schlickeiser, R., Reich, P., Pohl, M., Reuter, H.P., Kanbach, G., & Schönfelder, V. 1993, A&A, 273, 65
- Romanova, M.M., & Lovelace, R.V.E. 1997, ApJ, 475, 97
- Romney, J.D., et al. 1984, A&A, 135, 289
- Schalinski, C., Britzen, B., Witzel, A., Alef, A., & Campbell, J. 1993 in *Sub-arcsecond Radio Astronomy*, ed. R.J. Davis & R.S. Booth (Cambridge:Cambridge Univ. Press), 199
- Smith, A.G., Nair, A.D., Leacock, R.J., & Clements, S.D. 1993, AJ, 105, 437
- Stickel, M. & Kühr, H. 1994, A&AS, 105, 67
- Stickel, M., Rieke, G.H., Kühr, H., & Rieke, M.J. 1996, ApJ, 468, 556
- Tang, G., Rönnäng, B. & Bååth, L. 1989, A&A, 216, 31
- Tateyama, C.E., Kingham, K.A., Kaufmann, P., Piner, B.G., de Lucena, A.M.P., & Botti, L.C.L. 1998, ApJ, 499, in press
- Teräsraanta, H. & Valtaoja, E. 1994, A&A, 283, 51
- Thompson, D.J., et al. 1995, ApJS, 101, 259
- Thompson, D.J., et al. 1996, ApJS, 107, 227
- Tingay, S.J., et al. 1996, ApJ, 464, 170
- Tornikoski, M., Valtaoja, E., Teräsraanta, H., Smith, A.G., Nair, A.D., Clements, S.D., & Leacock, R.J. 1994, A&A, 289, 673
- Unwin, S.C., Wehrle, A.E., Urry, C.M., Gilmore, D.M., Barton, E.J., Kjerulf, B.C., Zensus, J.A., & Rabaca, C.R. 1994, ApJ, 432, 103
- Vermeulen, R.C. & Cohen, M.H. 1994, ApJ, 430, 467
- Vicente, L., Charlot, P., & Sol, H. 1996, A&A, 312, 727
- von Montigny, C., et al. 1995a, ApJ, 440, 525

- von Montigny, C., et al. 1995b, *A&A*, 299, 680
- Wagner, S., et al. 1995, *A&A*, 298, 688
- Wehrle, A.E., Cohen, M.H., Unwin, S.C., Aller, H.D., Aller, M.F., & Nicolson, G. 1992, *ApJ*, 391, 589
- Wehrle, A.E., Unwin, S.C., & Zook, A.C. 1996, in *Blazar Continuum Variability*, ed. H.R. Miller, J.R. Webb, & J.C. Noble (San Francisco:ASP), 430
- Xu, W., Readhead, A.C.S., Pearson, T.J., Wilkinson, P.N., & Polatidis, A.G. 1994, in *NRAO Workshop 23, Compact Extragalactic Radio Sources*, ed. J.A. Zensus & K.I. Kellermann (Green Bank:NRAO), 7
- Zensus, J.A., Cohen, M.H., & Unwin, S.C. 1995, *ApJ*, 443, 35
- Zensus, J.A., Porcas, R.W., & Pauliny-Toth, I.I.K. 1984, *A&A*, 133, 27
- Zensus, J.A., Unwin, S.C., Cohen, M.H., & Biretta, J.A. 1990, *AJ*, 100, 1777